Phase Change Materials and Their Application to Nonvolatile Memories

Simone Raoux,*,† Wojciech Wełnic,‡ and Daniele Ielmini§

IBM/Macronix Joint Project, IBM T. J. Watson Research Center, 1101 Kitchawan Road, P.O. Box 218, Yorktown Heights, New York 10598, Laboratoire des Solides Irradies, Ecole Polytechnique, 91128 Palaiseau, France, and Dipartimento di Elettronica e Informazione and the Italian Universities Nanoelectronics Team (IU.NET), Politecnico di Milano, piazza Leonardo da Vinci 32, 20133 - Milano (MI), Italy

Received February 2, 2009

Contents

1. Introduction

Phase change materials are materials that exist in at least two structurally distinct solid phases, an amorphous and one (or more) crystalline phases. Many materials display phase change properties in this sense and can be deposited at least as a thin film in an amorphous phase (low temperature deposition, very thin film) or crystalline phase (high temperature deposition, epitaxy). Often the amorphous and crystalline phases have very different optical and electrical properties stemming from the large differences in structure between the amorphous and the crystalline phases. These differences can be used to store information in technological applications if it is possible to switch the material repeatedly between the two phases and if both phases are stable at operating temperature. The transformation of the metastable amorphous phase to the energetically favorable, stable crystalline phase occurs by heating the material above its crystallization temperature for a time long enough for crystallization to occur. The reverse operation is performed by melting the crystalline material and quenching it fast enough so that it solidifies in the

Simone Raoux is a Research Staff Member at the IBM T. J. Watson Research Center. She received her M.S. degree in 1984 and her Ph.D. degree in physics in 1988, both from Humboldt University, Berlin, Germany. From 1988 to 1991 she worked as a Staff Scientist at the Institute for Electron Physics in Berlin, Germany, doing research in the field of electrical breakdown. From 1992 to 2000, she was a Staff Scientist at Lawrence Berkeley National Laboratory and performed research in the fields of vacuum arc deposition, ion implantation, photoemission electron microscopy, X-ray magnetic circular dichroism, and near-edge X-ray absorption fine structure spectroscopy. Her current research interests include the physics and materials science of phase change materials.

Wojciech Wełnic did his Ph.D. research at the Technical University Aachen between 2003 and 2006 working on optical and electronic properties of phase change materials. During his Ph.D. he went to the Forschungszentrum, Juelich, Germany, as well as to the Ecole Polytechnique in Paris, France, to study computational methods in solid state physics. Today he works as a postdoctoral fellow at the Ecole Polytechnique and the ESRF in Grenoble on electronic excitations and structural properties of phase change materials.

---

† IBM T. J. Watson Research Center.
‡ Ecole Polytechnique.
§ Politecnico di Milano.

10.1021/cr900040x

Daniele Ielmini received Laurea (cum laude) and Ph.D. degrees from the Politecnico di Milano, Italy, in 1995 and 1999, respectively. He has been an Assistant Professor at Dipartimento di Elettronica e Informazione, Politecnico di Milano, since 2002. In 2006 he was a Visiting Scientist at Intel Co., Santa Clara, and the Centre for Integrated Systems, Stanford University, Stanford, CA. His main research interest is characterization and modeling of nonvolatile memories, including phase-change memories and resistive-switching memories.

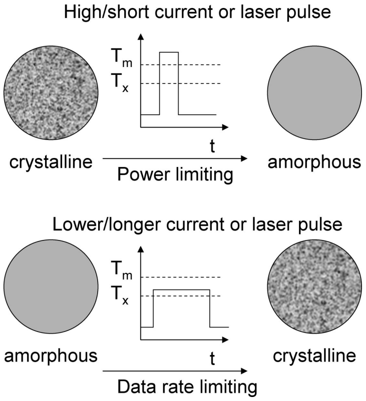

Figure 1. Schematic of the phase change processes. T_m is the melting temperature, T_x is the crystallization temperature, and t is the time.

amorphous state. Two main applications of phase change materials exist today: the mature rewritable optical phase change storage technology (rewritable compact discs—CDs, digital versatile discs—DVDs, and Blu-ray discs) and the emerging phase change random access memory (PCRAM) technology. The heating is done using a laser pulse in optical applications and a current pulse leading to Joule heating in PCRAM cells. The phase change switching principle is schematically shown in Figure 1. The crystallization is the data-rate limiting operation because it can take long times for some materials to crystallize whereas the melt-quenching needs to be inherently fast; otherwise, the material recrystallizes during cooling. The melt-quenching is the power limiting operation, since enough power needs to be delivered to heat the material above the melting temperature, which for phase change materials is typically between 500 and 800 °C.[1] The reading operation measures the reflectivity using a low power laser pulse in optical storage and the resistivity using a small current pulse in PCRAM, respectively. The read pulses are too low to cause any phase change.

A phase change material is useful for technological applications if it fulfills a large set of material requirements which depend on the application. These sets of parameters that need to be fulfilled simultaneously are quite difficult to achieve and sometimes seem contradictory. For example, storage technologies based on phase change materials require very fast (nanosecond time scale) crystallization of the amorphous phase during writing but very high stability of the amorphous phase against spontaneous crystallization (archival lifetime of 10 years). These are response times that differ by 17 orders of magnitude![2] For these reasons only very few materials are actually technologically useful phase change materials and it took decades between the discovery and proposal of phase change material based technology and the actual technological realization because the early phase change materials fulfilled only a subset of the requirements.

Optical data storage based on phase change materials started with the discovery of a certain family of phase change materials (semiconductor alloys containing Ge, Sb, and Te) that showed the required fast crystallization times that limit the data rate in optical storage. It is a mature technology today that has gone through several generations of products (rewritable compact discs—CD-RWs, digital versatile discs—DVD ± RW and DVD-RAM, and, most recently, Blu-ray discs—BD-RE). It triggered renewed interest in the development of solid state memory based on phase change materials—PCRAM. There is intense research and development effort at several companies and many universities to develop PCRAM. Plans for full flight production have been announced by BAE for a 4-Mbit memory chip targeted for space applications,[3] since PCRAM is inherently radiation hard. Phase change materials are one (if not the most) important issue in the PCRAM development; this is one of the reasons for this article in the current issue "Materials for Electronics".

This article will first describe the history of phase change materials. The second part of the paper is concerned with the properties of phase change materials. The structural properties of phase change materials are the reason for their distinct property differences, and they will be discussed in detail. The switching characteristics, such as crystallization speed, are of great importance for the technological applications and will be addressed afterward. Specific optical properties, such as large differences between the optical constants in the two phases, are required for optical storage, while a different set of materials parameters is necessary for a good PCRAM material (e.g., large difference between the resistivities of the two phases). The optical and electrical properties of phase change materials will be described in the next sections of the paper. A technology is only viable if it can be scaled to several future technology nodes (a semiconductor technology node is defined as the smallest half-pitch of contacted metal lines on any product fabricated by this technology).[4] It will be shown in this paper how material parameters change as dimensions shrink for phase change materials and to which dimension phase change technology can potentially be scaled down. The third part of the paper discusses phase change technologies: optical storage, PCRAM, and possible future applications of phase change materials such as dynamic RAM (DRAM), reconfigurable logic, or cognitive computing.

2. History of Phase Change Materials

Materials in distinct phases have been used in many technological applications. For example, carbon exists as diamond, graphite, carbon nanotubes, fullerenes, graphene, and amorphous, diamond-like carbon, and all these various forms of carbon have useful properties for one or the other application. To use a phase change material in two different

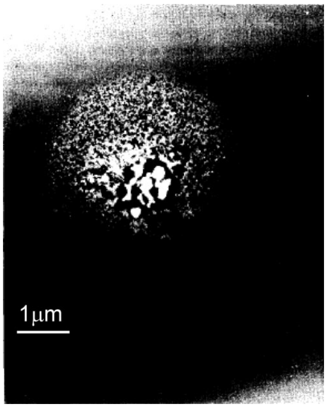

Figure 2. Electron micrograph of laser-induced crystallization of a 3-μm spot of an amorphous chalcogenide film. Reprinted with permission from ref 10. Copyright 1971 American Institute of Physics.

phases for technological applications was first proposed by Ovshinsky in 1968.[5] One of the most important properties of phase change materials (for PCRAM applications) is the so-called threshold switching, which will be described in detail in section 6.4. Threshold switching (without memory switching) was described for As−Te−I in 1964[6] and other alloys including As−Te−Se alloys in 1966.[7] Ovshinsky reported repeated threshold switching between a high resistive and a low resistive state using a material consisting of 48 atom % Te, 30 atom % As, 12 atom % Si, and 10 atom % Ge.[5] This alloy did not show memory switching either, but other alloys with reduced As content were reported to have memory switching effects.[5] He recognized the potential technological implications for data storage and described both threshold and memory switching and patented numerous possible device configurations for PCRAM in 1966.[8] His own view on the history of phase change materials can be found in ref 9.

The first optical switching of phase change materials was reported by Feinleib et al.[10] in 1971. Laser-induced switching of a $Te_{81}Ge_{15}Sb_2S_2$ film was demonstrated on the microsecond time scale. Figure 2 shows an electron micrograph of a crystalline spot produced by a laser pulse from ref 10. In 1978 data were reported by Burroughs Corporation about the prototype fabrication of a 1024-bit chip,[11] but this was never commercialized.

The main reason for the delay in commercialization was the slow crystallization speed of these early alloys in the micro- to millisecond range[12] and their limited cyclability. A major breakthrough was reached by the discovery of fast switching alloys on the pseudobinary line between GeTe and Sb_2Te_3 by Yamada et al.[13] These alloys showed large optical contrast over a wide range of wavelengths[14] and good cyclability[15] in addition to their short crystallization times. This discovery triggered the whole development of phase-change optical storage, which today is the most prevalent technology for rewritable media, with the rewritable Blu-ray disk being the latest product. The first product was introduced by Matsushita Electric (Panasonic Corporation) in 1990 with 500 MB capacity, with rewritable DVDs following in 1998 and Blu-ray discs in 2003.[16] Most of these products apply alloys based on the pseudobinary GeTe-Sb_2Te_3 materials, but a second class of alloys was also found to show fast switching: doped Sb_2Te. The dopants are often In and Ag, and these materials are also used in rewritable CDs, DVDs, and Blu-ray discs and were first introduced in 1997.[16]

This rapid and successful development in optical phase change technology triggered renewed interest in PCRAM technology. BAE Systems was one of the first companies starting in 1999 to develop PCRAM technology and has announced plans for large scale fabrication in 2009.[3] Many other companies, such as Samsung, Intel, IBM, Macronix, and STMicroelectronics (just to name a few),[16] started research and development programs in the early 2000s to fabricate PCRAM. The number of patents filed in the field has risen dramatically over the past few years, with more than 90% of all patents filed after 2000. The number has been above 100 per year since 2006.

Clearly, the development of new materials was the decisive factor for the development of optical phase change technology. Materials optimized for optical storage, however, are not necessarily optimum for PCRAM technology. Intense efforts are spent to better understand crystallization mechanisms and design new phase change materials for PCRAM based on this understanding.[16,17] This paper will summarize our current understanding of phase change material properties and describe their applications.

3. Structural Properties of Phase Change Materials

3.1. Structural Properties of the Crystalline State

Phase change materials show changes of their physical properties upon an amorphous to crystalline phase transition. The amorphous phase is characterized by high electrical resistivity and low optical reflectivity whereas the crystalline phase has low resistivity and high reflectivity. Hence, the structure within the different phases and particularly structural differences are of great importance in phase change materials. However, the structural properties in particular of the amorphous phase are very difficult to study. This phase not only lacks long-range order and periodicity, which are of great help for solid-state scientists in understanding material properties, it is furthermore very difficult to obtain quantities that are necessary for many experiments. This is because phase change materials are bad glass formers and hence crystallize easily rather than freeze in the glassy state. On one side, this is an important reason for the great interest in these materials, as it leads to fast phase transitions; on the other side, it complicates the structural analysis. Hence, many structural features of the amorphous phase have been revealed only recently or are still a subject of study.

In the following, the structural properties of some typical phase change materials are described in the crystalline, liquid, and the amorphous phases. The focus here is on compositions that lie on the pseudobinary line GeTe-Sb_2Te_3 (see Figure 3) because, as mentioned before, these materials enabled phase change optical storage technology.

Typical materials, such as $Ge_2Sb_2Te_5$, $Ge_1Sb_2Te_4$, GeTe, or Sb_2Te_3, show not only an amorphous−crystalline phase transition but also two different crystalline phases. This will be exemplified for the most simple phase change material, the binary composition GeTe. At high temperatures above 400 °C,[18] GeTe exhibits a rock-salt structure, as shown in Figure 4, which consists of two fcc sublattices shifted by half the lattice parameter in each direction (0.5 0.5 0.5) with respect to each other, and is described by the crystallographic

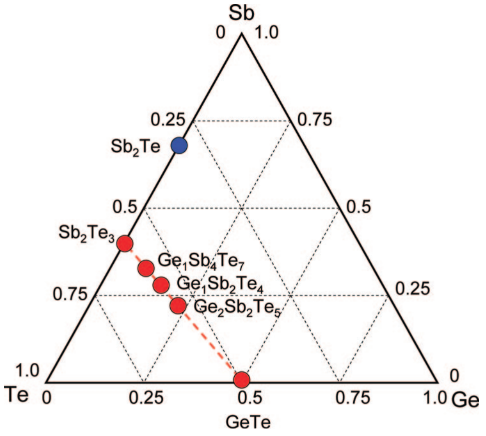

Figure 3. Many alloys which are applied as phase change materials lie on the GeTe-Sb$_2$Te$_3$ pseudobinary line. Another successful alloy is the eutectic composition Sb$_2$Te.

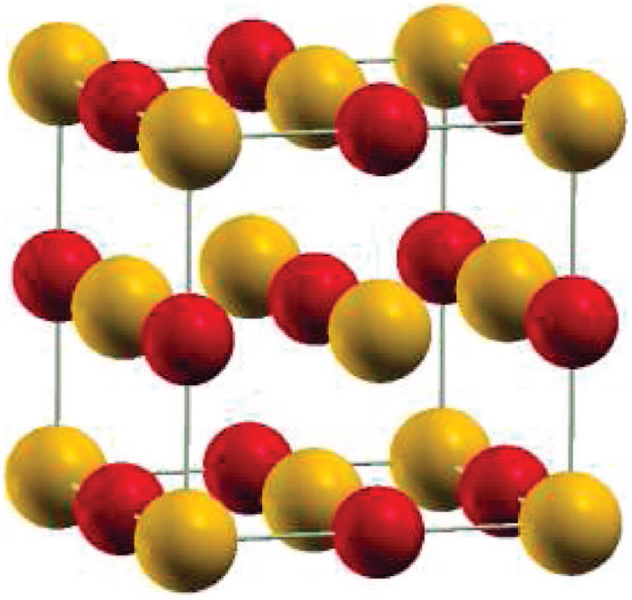

Figure 4. Rock-salt structure of GeTe. In ternary phase change materials (e.g., Ge$_1$Sb$_2$Te$_4$), one sublattice is statistically occupied by germanium, antimony, and vacancy sites.

space group $Fm3\bar{m}$ (No. 225). One sublattice is occupied by tellurium atoms, the other one by germanium atoms. At lower temperature, a rock-salt phase is also found as a so-called metastable phase after annealing amorphous GeTe thin films at ~180 °C. In fact, in the crucial phase transition employed in phase-change data storage, the material switches between the amorphous and the metastable rock-salt structure. However, in the ground state at lower temperatures, GeTe adopts a trigonal phase (space group $R3\bar{m}$, No. 166), which can be described as a rock-salt structure, slightly distorted by freezing in a TO-phonon along the [111]-direction (see e.g. ref 18). Figure 5 shows a comparison of the rock-salt and the trigonal phases in the primitive cell. Upon the phase transition to the trigonal structure, the unit cell is stretched along the ⟨111⟩-direction. Additionally, the central atom is displaced—also along the ⟨111⟩-direction from the center of the rhombohedron, which results in a geometry with alternating short and long bonds. Furthermore, it has been found that GeTe exhibits a large concentration of point defects. Ge-vacancies are known to be the dominant point defects (see e.g. ref 19 or 20) in this alloy.

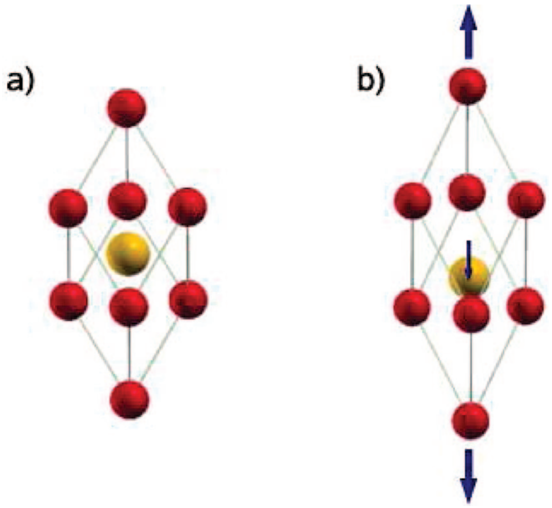

Figure 5. Rock-salt structure (a) and trigonal structure (b) of GeTe in the primitive unit cell. The trigonal structure is obtained by stretching the rock-salt cell along the ⟨111⟩-direction and shifting the central atom.

For the ternary alloys such as Ge$_2$Sb$_2$Te$_5$ and Ge$_1$Sb$_2$Te$_4$, the rock-salt structure has not been observed as a high temperature phase in bulk samples, as it was found in GeTe, but only as a metastable phase in thin films.[21] Here it is widely believed that one sublattice is occupied by tellurium atoms, the other one by a random distribution of germanium atoms, antimony atoms, and vacancy sites. However, recent results from *ab initio* calculations indicate that the occupation on the Ge/Sb-sublattice in ternary Ge—Sb—Te alloys might be ordered.[22] The most remarkable feature of this phase is the surprisingly high vacancy concentration of 25% on the Ge/Sb sublattice. This has been observed also for other alloys along the GeTe-Sb2Te$_3$ pseudobinary line.

The role of these vacancies for the stability of the structure and the electronic properties of the compound is still not fully understood. However, an important step in understanding the presence of the vacancies has been achieved recently. By employing *ab initio* calculations for fictitious systems along the stoichiometric line Ge$_1$Sb$_2$Te$_4$—Ge$_2$Sb$_2$Te$_4$ in the rock-salt phase, the influence of differences in the vacancy concentration on the electronic properties were studied numerically.[23] Ge$_1$Sb$_2$Te$_4$ contains 25% of vacancies on the Ge/Sb sublattice while in Ge$_2$Sb$_2$Te$_4$ all vacant lattice sites have been filled with Ge atoms. By studying the so-called chemical orbital Hamilton population (COHP),[24] bonding and antibonding contributions have been identified using these calculations. Figure 6 shows the COHP of the covalent Ge—Te and Sb—Te interactions in the three compounds Ge$_1$Sb$_2$Te$_4$, Ge$_{1.5}$Sb$_2$Te$_4$, and Ge$_2$Sb$_2$Te$_4$ both in the unrelaxed rock-salt lattice (top) as well as after the structural relaxation (bottom), which leads to local distortions of the lattice. The plot shows that the composition Ge$_2$Sb$_2$Te$_4$ exhibits a large degree of antibonding Ge—Te and Sb—Te interactions in the highest occupied bands close to the Fermi level. Thus, the composition Ge$_2$Sb$_2$Te$_4$ stands for a too high valence-electron concentration (VEC), which must be lowered to achieve better stability. This is achieved by removing atoms from the system. In these compounds, tellurium is the anionic atom with a high absolute electronegativity whose orbital contributions are dominant in the lower-lying valence bands. Hence, expelling Te atoms immediately weakens low-lying bonding states and is energetically unfavorable. Thus, Ge and Sb atoms whose orbitals both contribute to the states close to

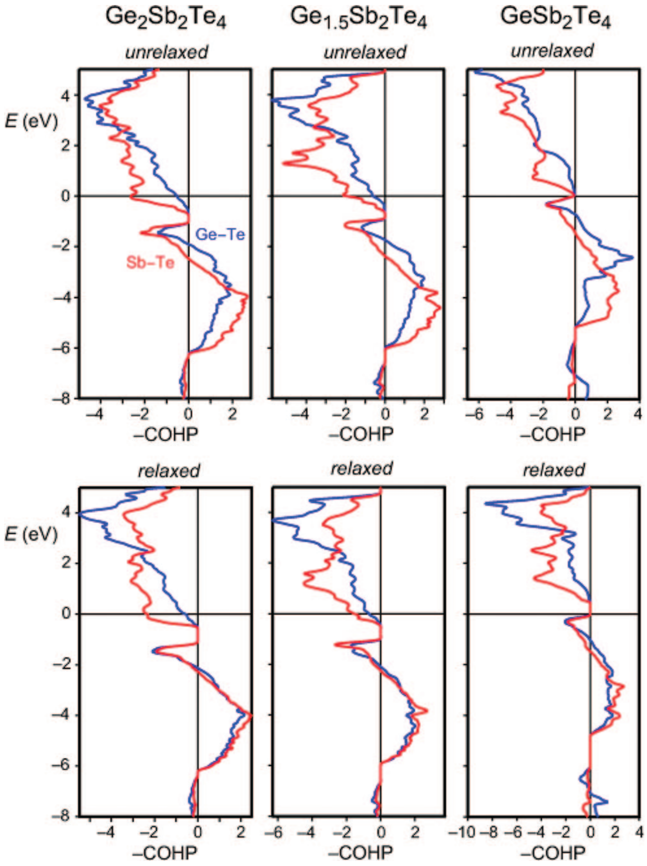

Figure 6. Crystal-orbital Hamilton population (COHP) bonding analysis: The plot displays the Ge−Te (blue) and Sb−Te (red) interactions in $Ge_2Sb_2Te_4$ (left), $Ge_{1.5}Sb_2Te_4$ (middle), and $Ge_1Sb_2Te_4$ (right); the upper panel shows the unrelaxed NaCl-lattice whereas the lower panel corresponds to the structure with full atomic relaxation. The Fermi levels are set to zero. Bonding interactions to the right, antibonding interactions to the left. Reprinted by permission from Macmillan Publishers Ltd.: Nature Materials (2007). From ref 23.

the valence band edge are energetically more favorable to remove. The comparison with the COHPs of the compositions $Ge_{1.5}Sb_2Te_4$ and $Ge_1Sb_2Te_4$ shows that these antibonding interactions are getting smaller and eventually vanish for an increasing number of vacancies. On the other hand, such a consecutive removal of Ge−Te bonds also decreases the degree of bonding states in the system. Thus, the most stable configuration with the lowest total energy is found for $Ge_{1.5}Sb_2Te_4$.[23]

In the ground state, Ge−Sb−Te alloys exhibit very complex, layered trigonal structures which are not yet fully revealed. With experimental methods it is very challenging to deduce the correct stacking order of the corresponding building blocks. Hence, density functional theory (DFT) calculations are employed to facilitate the structure determination of crystalline phase change materials. From studying the structural properties of $Ge_2Sb_2Te_5$ in the hexagonal phase, it has been suggested that the lowest total energy, i.e. the most stable phase, is found for a stacking order of Te−Ge−Te−Sb−Te−Te−Sb−Te−Ge- in the [0001]-direction.[22] This result agrees with a model based on electron microscopy measurements.[25] Agaev et al.[26] and Karpinsky et al.[27] suggested a geometry made of alternating GeTe and Sb_2Te_3-blocks as shown in Figure 7. However, recently Matsunaga and Yamada[21] suggested a slightly different stacking-order resembling the stable phase of $Pb_1Bi_2Se_4$.

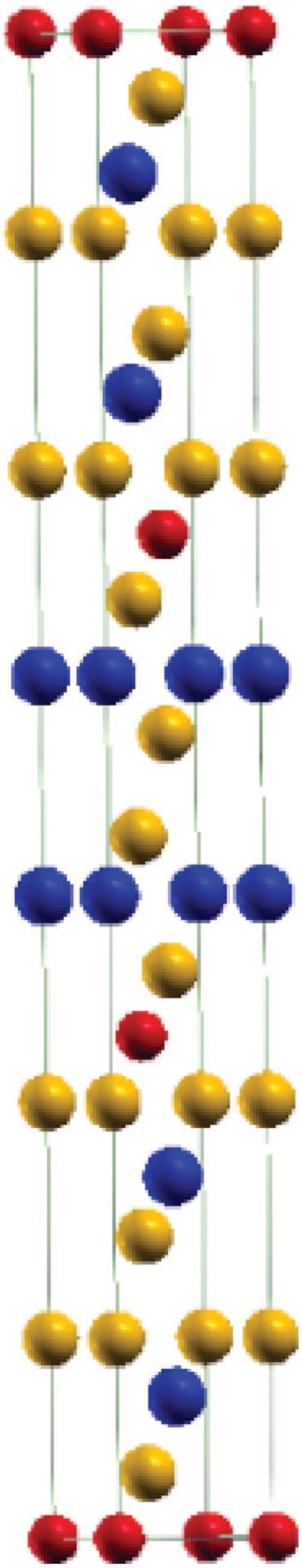

Figure 7. Crystalline structure of $Ge_1Sb_2Te_4$ according to Agaev et al.[26] and to Karpinsky et al.:[27] The unit cell exhibits trigonal symmetry (space group *R*_3*m*, No. 166) and consists of alternating blocks of GeTe and Sb_2Te_3 (Ge, red; Sb, blue; Te, yellow).

None of these models can be as easily related to the high-temperature rock-salt phase as in the case of GeTe. The phase transformation can only be achieved if atomic diffusion processes are present.[28] Particularly remarkable is the difference of these structures compared to the conventional semiconductors such as Si or GaAs, which show sp^3-hybridization and thus crystallize in a tetrahedral arrangement, resulting in the diamond (Si) or zinc blende (GaAs) structure. Phase change materials, however, show octahedral coordination, as in the rock-salt structure or in the distorted rock-salt coordination found in the stable trigonal phases of GeTe and $Ge_2Sb_2Te_5$. The origins of these characteristic structural arrangements are the bonding properties, which differ significantly from those of other semiconductors. Si or the III−V alloys exhibit strong sp^3-hybridization, which is not found in materials such as GeTe or $Ge_1Sb_2Te_4$, due to the large energy separation between the s- and the p-orbitals, originating from the higher Coulomb attraction of the nuclei of group VI-elements. Here the chemical bonding is mainly provided by the valence p-electrons;[29] the s-electrons do not participate in the bonding mechanism.[30] This leads to the octahedral structure as found in the crystalline state of phase change materials.[18,21] However, the structures also show that a rigid octahedral arrangement—which would result in a perfect rock-salt lattice—is not stable.[31] The alloys show distortions which lead to the trigonal ground states mentioned above. The underlying mechanism of these distortions is the Peierls mechanism.[32] The distortion leads to an opening of the electronic band gap due to symmetry breaking. The gain in electronic energy upon opening the gap is larger than the increased elastic energy in the distorted system; hence, the total energy decreases and the distorted system remains stable.

Gaspard et al. found that, for a number of ternary compounds containing group IV, V, and VI elements such as $Ge_5As_2Te_8$, the structure can be explained by a Peierls distortion.[29] This distortion has only been identified for p-bonded systems. Covalent materials, which exhibit a tetrahedral configuration and thus four nearest neighbors attributed to sp^3-hybridized orbitals, do not experience a minimization of the electronic energy upon a structural distortion. For group IV elements or III−V and II−VI semiconductors, this is again in line with the octet rule, which predicts four nearest neighbors for these alloys. Furthermore, this study showed that in various compounds composed of group V and group VI elements, the coordination number follows the octet rule using the average valence electron number.

In contrast to the classical Peierls distortions described above for the one-dimensional case, in some chalcogenides, the undistorted phase is semiconducting and not metallic. GeTe, for example, is reported to exhibit a band gap of 0.1−0.15 eV[33,34] in the rock-salt phase. However, this band gap widens in the distorted structure, resulting in a gap of 0.73−0.95 eV[35] for the trigonal phase of GeTe. The gap in the rock-salt phase cannot be solely explained by the covalent bonding of p-electrons. As the p-orbitals are half-filled, a covalent model would lead to a metallic phase. On the other side, such a gap can be explained in an ionic picture by assuming that the Ge 4p-electrons are transferred to the tellurium in order to fill the Te 5p-orbital. Therefore, this transfer generates an empty Ge 4p shell and a filled Te 5p shell with distinct energy which opens a gap between these two levels. However, the small differences in electronegativity of 2.01 for Ge compared to 2.10 for Te on the Pauling scale[36] indicate that the ionic contribution only plays a minor role in the bonding of GeTe.

In particular, one should note that the bonding properties described here provide an explanation for the instability of the regular, undistorted rock-salt structure of the alloys on the GeTe−Sb_2Te_3 pseudobinary line. The trends in this structural instability have been found to correlate fully with the trends in LO-TO splitting[37] for IV−VI compounds. It increases with increasing structural instability. Furthermore, the LO−TO splitting also reflects the trend in metallicity: with smaller band gaps, the dielectric constant increases, resulting in screening of the long-range interatomic interactions. Thus, it provides a useful single parameter for the prediction of spontaneous distortions in rock-salt chalcogenides.

3.2. Structural Properties of the Amorphous and Liquid States

A general characteristic attribute of the amorphous and the liquid structure is the lack of long-range order and periodicity. Therefore, neither a unit cell as given in the crystalline state can be defined, nor can the atomic positions within such a unit cell. Thus, this lack of long-range order significantly complicates a precise identification of the structural properties of these two phases. Nonetheless, average, statistical properties such as the structure factor or correlation functions are successfully employed to determine and classify the structure of amorphous solids and liquids by analyzing their short and medium range structural order.

To further characterize the amorphous state, the network connectivity is employed (see e.g. ref 38). In this model, the network is characterized by the number of constraints N_c, i.e. by bond-bending and bond-stretching forces. This number is related to the number of degrees of freedom N_d. Three different cases can be distinguished. In the first case, if $N_c < N_d$, the underconstrained glassy network is floppy and can freely crystallize. If $N_c > N_d$, the network is rigid and stressed and can relieve the stress by crystallizing exothermally. If $N_c = N_d$, one obtains an “ideal” network, which is rigid and yet stress-free.[39−41] In fact, subsequent work has confirmed the existence of such a stiffness transition at or very close to $N = 2.4$, e.g. for $Sn_xGe_{1-x}Se_2$ ($0 < x < 0.35$).[42] However, recently it has been found that there could be two closely spaced transitions rather than just one. For $Ge_xAs_xSe_{1-2x}$, these transitions occur at $N = 2.29$ and $N = 2.52$[43] and enclose an intermediate phase, which exhibits unusual properties. For instance, in contrast to systems outside the intermediate region, networks inside it do not show any aging; that is, there are no changes in the nonreversible enthalpy of the glass transition over a period of years.[39] Many chalcogenide compounds have been identified as intermediate glasses; however, for typical phase change materials such as ternary Ge−Sb−Te alloys, no studies regarding the network connectivity can be found in the literature.

Besides experimental methods such as neutron diffraction or EXAFS (extended X-ray absorption fine structure) spectroscopy, molecular dynamics and, recently, *ab initio* molecular dynamics have been employed in order to study the amorphous and liquid phases of a wide range of elements and alloys. In particular, these methods allow a detailed analysis of the local structural properties and the relationship between structural and electronic properties. Kresse and Haffner for example investigated the liquid−amorphous transition in Ge and the defect properties of the amorphous state of germanium.[44] Chelikowsky et al. studied the microstructure and the dynamical properties of several elements

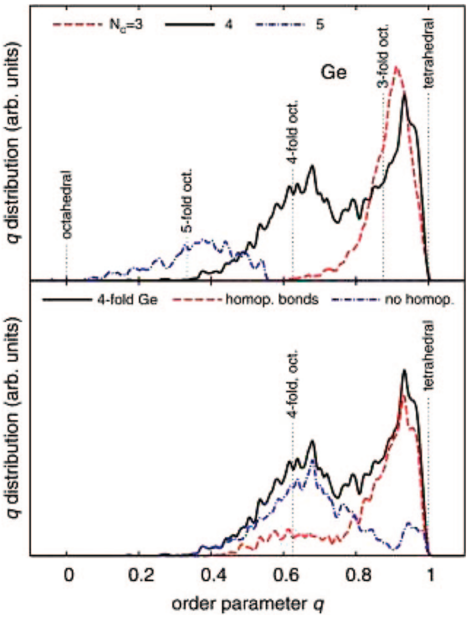

Figure 8. Distribution of the local order parameter *q* for Ge with different coordination numbers N_c. $q = 1$ for the ideal tetrahedral geometry, $q = 0$ for the six-coordinated octahedral site, and $q = {}^5/_8$ for a four-coordinated defective octahedral site. Top panel: *q*-distribution resolved for Ge with different coordination number. Bottom panel: *q*-distribution for four-coordinated Ge further resolved for Ge with at least one homopolar bond, with Ge or Sb bonding with Te, only no homopolar bonds. Reprinted with permission from ref 50. Copyright 2007 American Institute of Physics.

and alloys including Si, Ge, GaAs, and GeTe in the liquid phase.[45,46] For chalcogenide glasses, Li et al. identified the structural elements in amorphous As_2Se_3 and As_4Se_4.[47] Their calculations yielded a hierarchy of structural units, network inhomogeneities, and structural defects. $AsSe_3$ pyramids and As-$AsSe_2$ or Se_2As-$AsSe_2$ have been identified as the dominant building blocks in Se-rich regions and As-rich regions, respectively.

Structural properties of glassy binary IV−VI alloys have also been studied;[48,49] however, only recently, molecular-dynamics simulations of amorphous GeTe or ternary Ge−Sb−Te-alloys have become feasible, thanks to massively improved computer performance.[50–52] The analysis of these calculations results in a very detailed model of the local structure of amorphous $Ge_2Sb_2Te_5$.[50] After verifying that the structure factor of the calculated system agrees well with experimental data, a detailed account of the local bonding coordination for each atom type can be provided. It is found that Ge and Sb atoms have four nearest neighbors while Te exhibits three nearest neighbors. The bond angles have maxima mainly at 90 and 180 deg, recalling the distorted rock-salt environment found in the metastable crystalline phase. However, 38% of the Ge atoms are tetrahedrally coordinated, in particular if homopolar bonds are present. This can be analyzed using a local order parameter *q*,[53] where the sum runs over the couples of atoms bonded to a central atom j (see Figure 8). Further information is then obtained from an analysis of the ring structures in amorphous GeTe and $Ge_2Sb_2Te_5$.[51] 4-fold rings are found to be the dominant ring structure in $Ge_2Sb_2Te_5$. Most of these rings are of ABAB alternation with A = Ge and/or Sb and B = Te. This is also true for GeTe; however, in this case no clear maximum for any *n*-fold ring configuration can be identified. Furthermore, the molecular dynamics calculations reveal the vacancy structure in the amorphous alloys. It is found that cavities or voids occupy a total volume of 11.8% in $Ge_2Sb_2Te_5$ and 6.4% in GeTe, respectively. The vacancies, which tend to be surrounded by Te atoms, repel each other. Hence, only a few di- or multivacancies are identified. These findings allow for an interpretation of the phase transition process. The study suggests that it can be viewed as a vacancy-supported reorientation of ABAB-rings. As there are more ABAB-rings and fewer homopolar bonds in $Ge_2Sb_2Te_5$ compared to GeTe, the crystallization process is facilitated in the ternary alloy.

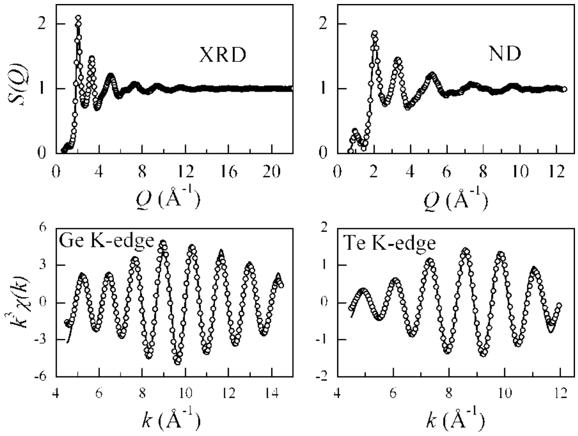

Figure 9. XRD and neutron diffraction structure factors, and EXAFS spectra for as-sputtered amorphous $Ge_1Sb_2Te_4$. Circles, measured; lines, obtained by simultaneous RMC simulation of the experimental XRD, ND, and EXAFS data. Reprinted with permission from ref 56. Copyright 2008 by the American Physical Society.

Experimentally it has been particularly cumbersome to determine the amorphous structure. As the materials recrystallize easily, it is very difficult to obtain a sufficiently large amount of amorphous material as needed for experimental techniques such as neutron diffraction. EXAFS measurements have been identified as a promising technique to solve this problem, as they can be performed with amorphous thin film samples, which are easily prepared, e.g. by sputter deposition. Recent publications of EXAFS data[54,55] revealing the local order of amorphous GeTe and $Ge_2Sb_2Te_5$ have led to a remarkable paradigm shift for phase change alloys. The data showed that the local order in the crystalline and amorphous states of these materials is very different: The germanium atoms which occupy octahedral positions in the crystalline phase switch to a tetrahedral coordination in the amorphous phase. This study has triggered many further experimental investigations of the amorphous phase.

The most detailed and most profound have been provided by Jovari et al.[56,57] The authors studied the local atomic order in $Ge_2Sb_2Te_5$ and $Ge_1Sb_2Te_4$ by combining EXAFS and X-ray and neutron diffraction with a reverse Monte Carlo analysis (RMC)[56,57] (see Figure 9). RMC usually has to be used with great caution, as it is a purely mathematical method and might thus produce unphysical results. However, the large amount of different data from different experimental methods used for fitting the RMC simulations by Jovari et al. decreases these risks substantially. Hence, these studies provide the most systematic and in-depth experimental investigation of the amorphous structure of phase change materials. They reveal that, in $Ge_2Sb_2Te_5$ and $Ge_1Sb_2Te_4$, Ge−Ge and Ge−Sb bonds are present, in contrast to the crystalline phase, while Te−Te and Sb−Sb bonds are negligible. Furthermore, the local coordination of the different elements follows the “8 − *N*-rule”; that is, Te has on average two nearest neighbors, Sb three, and Ge four. Furthermore, it has been found that no dominant building blocks are present in the amorphous phase, while the Ge atoms are mainly tetrahedrally coordinated again, in contrast to the crystalline phase, where they are octahedrally coordinated. Another characteristic feature of phase change materials is given by the large volume increase upon amorphization. For GeTe it amounts to 5−10%,[58] and for ternary Ge−Sb−Te alloys 6−10% has been measured.[59,60] As 4-fold tetrahedral coordination requires a larger volume than octahedral coordination, this increase can be attributed to the change in local order.

Remarkably for the liquid phase of GeTe and $Ge_{15}Te_{85}$, a structural model has been proposed which differs from the “tetrahedral short range order” model for amorphous $Ge_2Sb_2Te_5$. Neutron scattering and *ab initio* molecular dynamics calculations have been employed to study the liquid structure of GeTe and revealed a high degree of alternating chemical order with increasing temperature.[46] The structure of the liquid has been described to be driven by a reentrant Peierls distortion, exhibiting short and long bonds, similar to the trigonal crystalline ground state of GeTe. For liquid $Ge_{15}Te_{85}$, Bichara et al. also observed a Peierls transition using neutron scattering, EXAFS, and *ab initio* molecular dynamics calculations.[61] No such studies are available in the literature for the liquid phase of ternary phase change materials, such as $Ge_2Sb_2Te_5$ or $Ge_1Sb_2Te_4$. Furthermore, in the literature no evidence for this structural model is found for the amorphous phase of any chalcogenide or phase-change alloy. As both models, the tetragonal short-range order as well as the Peierls transition, imply a shift of Ge atoms along the ⟨111⟩-direction, further studies are necessary to reveal the difference between these models. These studies should also help to clarify which model applies to a certain compound, and by making comparisons between measurements of liquid and amorphous phases, they should reveal if there are any substantial differences between the structures of these two phases.

4. Switching Kinetics of Phase Change Materials

The crystallization time of phase change materials is the data-rate-limiting process in technological applications and thus a very important parameter. The driving force for crystallization is the difference between the Gibbs free energy between the amorphous (solid or liquid) phase and the crystalline phase. The first step for crystallization is the crystal nucleation, either inside the amorphous phase (homogeneous nucleation) or at the interface of the amorphous phase with another material or at an impurity (heterogeneous nucleation). In practical cases, both homogeneous and heterogeneous nucleations occur simultaneously. The heterogeneous nucleation rates can be orders of magnitude higher than the homogeneous nucleation rate,[62] and therefore, heterogeneous nucleation often dominates the nucleation process; that is, the crystal formation starts at surfaces, interfaces, or impurities.[63,64] For homogeneous nucleation, according to the classical nucleation theory,[65] crystal clusters have a size distribution given by Boltzmann’s statistics

$$N^{\mathrm{equ}}(r) = N_0 \exp\left(-\frac{\Delta G^{\mathrm{hom}}_{\mathrm{cluster}}(r)}{kT}\right) \tag{1}$$

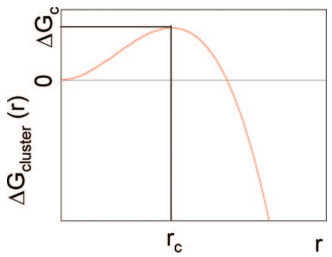

Figure 10. Reversible work for formation of clusters with radius r, $\Delta G_{\mathrm{cluster}}(r)$. r_c is the critical radius. Clusters grow for $r > r_c$ and decay for $r < r_c$.

where N^{equ} is the number of clusters of radius r at equilibrium and N_0 is the total number of atoms, both normalized per unit volume, $\Delta G^{\mathrm{hom}}_{\mathrm{cluster}}(r)$ is the reversible work for crystal cluster formation, k is the Boltzmann constant, and T is the temperature. The reversible work for cluster formation, $\Delta G^{\mathrm{hom}}_{\mathrm{cluster}}(r)$, is determined by two forces. The first is the energy gained by forming the crystal phase; the second is the energy required for forming the interface between the crystalline cluster and the amorphous phase. $\Delta G^{\mathrm{hom}}_{\mathrm{cluster}}(r)$ can be expressed by[62]

$$\Delta G^{\mathrm{hom}}_{\mathrm{cluster}}(r) = -\Delta G_{\mathrm{ac}}\frac{4}{3}\pi r^3 + \sigma_{\mathrm{ac}}4\pi r^2 \tag{2}$$

where ΔG_{ac} is the Gibbs free energy difference between the amorphous and crystalline phases (per unit volume) and σ_{ac} is the amorphous−crystalline interfacial free energy. For small cluster radii, the second term is larger, energy is needed to form the cluster, their formation is energetically unfavorable, and they decay. Above a critical cluster size r_c[62]

$$r_c = 2\sigma_{\mathrm{ac}}/\Delta G_{\mathrm{ac}} \tag{3}$$

the first term dominates, energy is gained when the cluster is formed (more atoms are added to it), and the cluster grows. Figure 10 shows ΔG_{ac} as a function of r. At $r = r_c$, the critical work of cluster formation, $\Delta G^{\mathrm{hom}}_{c}(r)$, is[62]

$$\Delta G^{\mathrm{hom}}_{c} = \frac{16}{3}\frac{\sigma_{\mathrm{ac}}{}^3}{(\Delta G_{\mathrm{ac}})^2} \tag{4}$$

Experimental observation indicates that crystallization occurs preferably at interfacial boundaries.[62] This is attributed to differences between the interfacial energies of the amorphous and crystalline phases and the substrate. This heterogeneous nucleation is modeled by the spherical cap model. It is assumed that the crystal has the shape of a spherical cap[66] with a volume V_{sc} of

$$V_{\mathrm{sc}} = \frac{4}{3}\pi r^3 f(\theta) \tag{5}$$

with

$$f(\theta) = \frac{(2 + \cos\theta)(1 - \cos\theta)^2}{4} \tag{6}$$

and θ being the wetting angle (Figure 11). Equation 2 now needs to be replaced by[66]

$$\Delta G^{\mathrm{het}}_{\mathrm{cluster}}(r) = -\Delta G_{\mathrm{ac}}\frac{4}{3}\pi r^3 f(\theta) + \sigma_{\mathrm{ac}}4\pi r^2\frac{1 - \cos\theta}{2} + \pi(r\sin\theta)^2(\sigma_{\mathrm{cs}} - \sigma_{\mathrm{as}}) \tag{7}$$

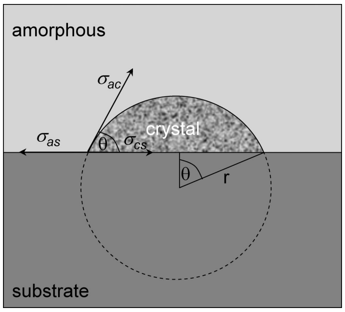

Figure 11. Spherical cap model for heterogeneous cluster formation. The crystal is assumed to have the shape of a spherical cap. θ is the wetting angle, and σ_{as}, σ_{ac}, and σ_{cs} are the interfacial energies between the amorphous (a) and crystalline (c) phases and the substrate (s).

where $\Delta G^{het}_{cluster}(r)$ is the reversible work for heterogeneous cluster formation and σ_{as} and σ_{cs} are the amorphous−surface and crystal−surface interfacial free energies. Because

$$\sigma_{cs} - \sigma_{as} = -\sigma_{ac}\cos\theta \tag{8}$$

it follows that the critical work of heterogeneous cluster formation, ΔG^{het}_c, is reduced by $f(\theta)$ compared to the homogeneous case

$$\Delta G^{het}_c = f(\theta)\Delta G^{hom}_c \tag{7a}$$

The critical radius is the same for both cases, but the number of atoms in the critical cluster is reduced by $f(\theta)$ for heterogeneous nucleation.

Classical nucleation theory assumes that clusters evolve by the addition of atoms to or removal of atoms from the cluster. Additional assumptions later introduced to the model include an equal probability of critical clusters to grow or shrink, and a finite probability of supercritical clusters to still decay even though they are much more likely to grow.[62,67] Early models assumed a cluster distribution according to eq 1 with $N^{equ}(r) = 0$ for $r > r_c$, since the model becomes unphysical for larger r. With a more realistic steady-state cluster distribution $N^{ss}(r)$ that assumes $N^{ss}(r_c) = {}^1/_2 N^{equ}(r_c)$ at r_c, shows a gradual reduction of $N^{ss}(r)$ to zero for $r > r_c$, and approaches $N^{equ}(r)$ for $r < r_c$, the following steady-state nucleation rate I^{ss} can be derived[62,67]

$$I^{SS} = \varepsilon s_c \gamma N_0 \Gamma_z \exp\left(-\frac{\Delta G^{hom}_c f(\theta)}{kT}\right) \tag{8a}$$

ε is a factor taking into account that in the case of heterogeneous nucleation only a fraction of all atoms N_0 is in contact with the heterogeneity and can contribute to nucleation ($\varepsilon \ll 1$ for heterogeneous nucleation; $\varepsilon = 1$ for homogeneous nucleation). s_c is the number of surface atoms in the critical cluster, and γ is the arrival rate of atoms in the amorphous phase at the critical (crystalline) cluster surface and is assumed to be[68]

$$\gamma = \frac{6D}{\lambda^2} \tag{9}$$

for a diffusion-limited crystallization, which is typical for phase change materials. D is the diffusivity of the amorphous phase, and λ is the average interatomic distance. Γ_z is the so-called Zeldovich factor[67]

$$\Gamma_Z = \frac{1}{n_c}\left(\frac{\Delta G_c}{3\pi kT}\right)^{1/2} \tag{10}$$

where n_c is the number of atoms in the critical cluster. Γ_z is weakly temperature dependent and between 0.1 and 0.001 in most cases. D is related to the viscosity η via the Stokes−Einstein equation

$$D = \frac{kT}{3\pi\lambda^3\eta} \tag{11}$$

ΔG_{ac} has been estimated by

$$\Delta G_{ac} = \Delta H_f F_T \tag{12}$$

where ΔH_f is the enthalpy of fusion. Various approximations have been proposed: $F_T = (T_m - T)/T_m$;[69] $F_T = 2T(T_m - T/T_m)/(T_m + T)$;[70] $F_T = T(T_m - T/T_m)/T_m$;[71] $F_T = 7T(T_m - T/T_m)/(T_m + 6T)$,[72] where T_m is the melting temperature.

We have calculated I^{ss} for the most commonly studied phase change material $Ge_2Sb_2Te_5$ following the assumptions made in refs 70, 72, and 73. The viscosity η was modeled by an Arrhenius equation $\eta = A\exp(E_\eta/kT)$[74,75] below the glass transition temperature T_g with an exponential factor of $E_\eta = 1.76$ eV,[75] and following a Vogel−Fulcher−Tamann ansatz[75] $\eta = \eta_0\exp[B/(T - T_0)]$ above T_g. The constants A, B, η_0, and T_0 where selected to fulfill the following conditions[73] for η: $\eta(T_g) = 10^{12}$ Pa s, $\eta(T_m) = 2 \times 10^{-2}$ Pa s, and $m = 45$, where m is the fragility index[76]

$$m = \left.\frac{\partial \log_{10}\eta(T)}{\partial(T_g/T)}\right|_{T=T_g} \tag{13}$$

Values for σ_{ac} and ΔH_f were also taken from ref 73.

Figure 12 shows I^{ss} for homogeneous nucleation (solid lines) and for heterogeneous nucleation (dashed lines) for different wetting angles θ. For low T, I^{ss} is smaller for heterogeneous nucleation than for homogeneous nucleation because $\varepsilon \ll 1$ (we assumed $\varepsilon = 0.006$, a 100 nm thick film with two interfaces). At high T close to the melting temperature, the heterogeneous I^{ss} is many orders of magnitude larger than the homogeneous I^{ss} for small wetting angles. The experimental observation of heterogeneous nucleation rates that are much larger than homogeneous nucleation rates implies small wetting angles. In particular, the assumed values of the interfacial free energy have a very strong influence on the nucleation rate and can change it by many orders of magnitude.

Besides the strong dependence of the values of I^{ss} on the wetting angle and the interfacial free energy, the temperature of the maximum of I^{ss} depends on θ as well (Figure 12), and these are indications that the nature of interfaces and heterogeneities can have a very large influence on the crystallization as it is observed experimentally.

The steady state of nucleation is reached after an incubation time τ that was estimated by Kashchiev[77] to be

$$\tau = \frac{4}{\pi^3 s_c \gamma \Gamma_z^2} \tag{14}$$

and is shown in Figure 13 as a function of temperature for $Ge_2Sb_2Te_5$ (from ref 74 assuming an Arrhenius-type dependence of the viscosity with an exponential factor of $E_\eta = 2$ eV). The strong temperature dependence is due to the strong

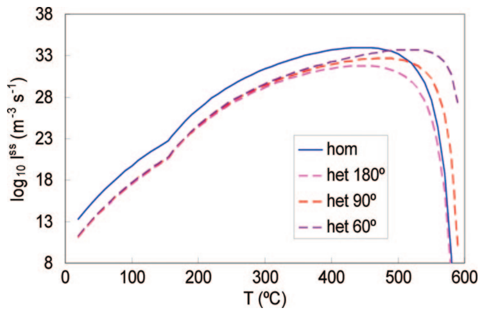

Figure 12. Calculated steady-state homogeneous (hom, solid line) and heterogeneous (het, dashed lines) nucleation rates I^{ss} for various wetting angles as a function of temperature; eq 8.

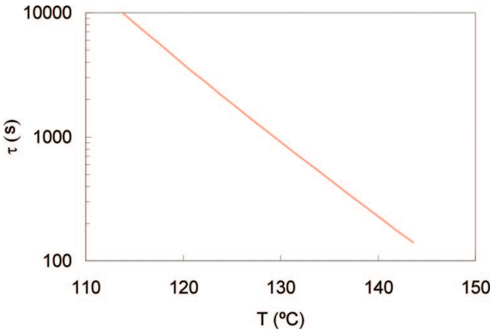

Figure 13. Calculated incubation time τ for homogeneous nucleation as a function of temperature T; eq 14. Reprinted with permission from ref 74. Copyright 2004 American Institute of Physics.

temperature dependence of the viscosity, which factors into γ (eqs 9 and 11). It is clear that τ can be much longer than technologically relevant time scales, which are in the nanosecond range. In this case, numerical models need to be applied that treat transient effects properly.[74]

The second step of the crystallization process is the growth of supercritical crystalline nuclei to macroscopic size. For phase change materials, the crystal growth is interface-controlled. Atoms move from the amorphous phase to the supercritical crystalline cluster containing n ($n > n_c$) atoms by diffusive jumps with the arrival rate γ and are added to the cluster at a rate ν_n^+ proportional to the available attachment sites (surface atoms) $s = 4n^{2/3}$. They move over the energy barrier ΔG^* of the "activated complex"[68] with an attempt frequency ω

$$\nu_n^+ = s\gamma = s\omega \exp\left(-\frac{\Delta G^*}{kT}\right) \tag{15}$$

The reverse process of removal of an atom from a cluster with $n + 1$ atoms is then given by

$$\nu_{n+1}^- = s\omega \exp\left(-\frac{\Delta G^* + (\Delta G_{\text{cluster},n} - \Delta G_{\text{cluster},n+1})}{kT}\right)$$
$$= s\gamma \exp\left(-\frac{(\Delta G_{\text{cluster},n} - \Delta G_{\text{cluster},n+1})}{kT}\right) \tag{16}$$

where $\Delta G_{\text{cluster},n}$ and $\Delta G_{\text{cluster},n+1}$ are the Gibbs free energies of clusters of size n and $n + 1$, respectively. The difference between ν_n^+ and ν_{n+1}^- is the growth rate $\partial n/\partial t$ of the cluster, which is related to the crystal growth velocity u by

$$u = \frac{\partial r}{\partial t} = \frac{\partial r}{\partial n}\frac{\partial n}{\partial t} = (\nu_n^+ - \nu_{n+1}^-)\frac{V_{\text{atom}}}{4\pi r^2} \tag{17}$$

where V_{atom} is the volume of the atom. Using eq 2, a crystal growth velocity u can be approximated by

$$u = \frac{2}{3}\lambda\gamma\left[1 - \exp\left(-\frac{V_{\text{atom}}\Delta G_{\text{ac}}}{kT}\left[1 - \frac{r_c}{r}\right]\right)\right] \tag{18}$$

For cluster radii $r \gg r_c$, it becomes constant in time (for a given temperature), and indeed constant crystal growth velocities have been observed experimentally.[64,78] The crystal growth velocity has a maximum close to the melting temperature (at higher temperature than the maximum of the nucleation rate) but then falls to zero at the melting temperature.

Nucleation rates and crystal growth velocities were measured using atomic force microscopy (AFM), utilizing the reduced height of crystalline areas caused by the increase in mass density upon crystallization.[64,78] Various alloys were studied: Ag- and In-doped Sb_2Te (AIST), which is applied in optical storage (composition $Ag_{0.055}In_{0.065}Sb_{0.59}Te_{0.29}$), and several Ge−Sb−Te alloys ($Ge_4Sb_1Te_5$, $Ge_2Sb_2Te_5$, and $Ge_1Sb_2Te_4$). Phase change materials are categorized into nucleation-dominated and growth-dominated materials. Nucleation-dominated materials have relatively short incubation times, high nucleation rates, but slow growth velocities while growth-dominated materials have relatively long incubation times, low nucleation rates, and high growth velocities. Since the ratios between these processes depend on the temperature, it is possible for the same material to behave like a nucleation-dominated material at low temperature (near the peak of the nucleation rate, Figure 12) but like a growth-dominated material at high temperature near the peak of the crystal growth velocity. This was, for example, shown for AIST.[79]

Figure 14 (from ref 78) demonstrates convincingly the difference between growth-dominated AIST and nucleation-dominated Ge−Sb−Te alloys. It shows AFM images acquired after heating the material for different durations and at different temperatures. While AIST shows crystals (dark areas, low because of mass density increase) of very similar size which all nucleate at about the same time and then grow rapidly, the Ge−Sb−Te alloys show crystals of very different sizes. The growth for these alloys is so slow that nucleation of new crystals occurs simultaneously with growth of "older" crystals (which is always true for all materials but due to the different time scales of the processes leads to phenomenologically different crystallization behavior). From these AFM images, nucleation rates and crystal growth velocities where determined as a function of temperature. The results are characteristic for a heterogeneous nucleation process, since transmission electron microscope studies confirmed the nucleation only at the sample surfaces.[63,64] It was found that in the temperature range observed (between 90 and 180 °C depending on the material) both the nucleation rate and growth velocity increased with temperature and the growth velocity was found to be independent of time,[64,78] so the observed crystals were much larger than the critical clusters, which are only about 1 nm in this temperature range. It was found that AIST has a much lower nucleation rate than Ge−Sb−Te alloys and a much longer incubation time τ. The incubation time was so long that no steady-state nucleation rate I^{ss} was reached. For the Ge−Sb−Te alloys, I^{ss} was fit

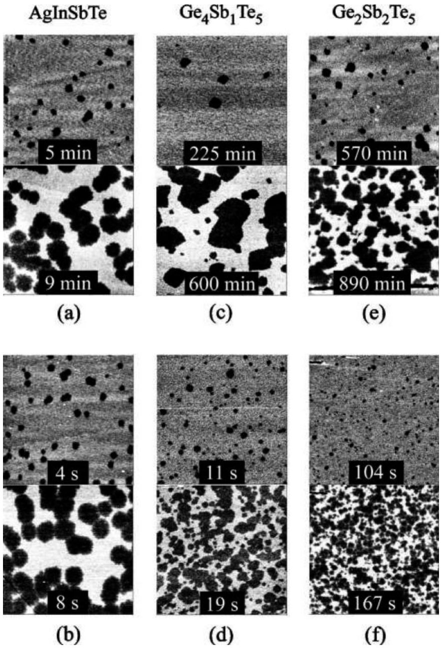

Figure 14. AFM scans (field of view 3 μm × 3 μm) of various phase change materials after various heating times (total times including preceding anneals). The dark areas are crystalline (high mass density), the bright areas amorphous (low mass density). (a) AIST 160 °C; (b) AIST 180 °C; (c) $Ge_4Sb_1Te_5$ 140 °C; (d) $Ge_4Sb_1Te_5$ 180 °C; (e) $Ge_2Sb_2Te_5$ 115 °C; (f) $Ge_2Sb_2Te_5$ 145 °C. Reprinted with permission from ref 78. Copyright 2004 American Institute of Physics.

to an Arrhenius equation ($I^{ss} \propto \exp(-E_I{}^{ss}/kT)$; see eq 8, and the activation energies $E_I{}^{ss}$ for nucleation were determined. $Ge_1Sb_2Te_4$ showed the lowest $E_I{}^{ss}$ of 2.82 eV while $Ge_4Sb_1Te_5$ showed the highest of 4.09 eV.

Measured crystal growth velocities were between tens of nm/s and a few pm/s; they were also fit to an Arrhenius equation [$u \propto \exp(-E_u/kT)$; see eq 18], and the activation energy for crystal growth E_u was found to be between 1.89 eV for $Ge_1Sb_2Te_4$ and 2.90 eV for AIST.

Much faster crystal growth velocities are observed in static laser tester experiments.[79] In these experiments, thin films of phase change materials are exposed to laser pulses of variable power and duration and the increase in reflectivity that accompanies crystallization or the decrease that accompanies melt-quenching is measured as an indication of phase change. To measure only the crystal growth velocity without the influence of incubation and nucleation, a film is first heated above its crystallization temperature to fully crystallize it. It is then exposed in the same location to first a pulse (high power, short) that will melt-quench (amorphize) the material. A second pulse of variable power and duration is then applied in an attempt to recrystallize the material by growing the crystals from the amorphous−crystalline interface without need of nucleation. For growth-dominated materials, the recrystallization occurs indeed from the border and the crystal grows inward, leaving an amorphous area in the center if the laser pulse was too short or too low.[79] For this case, the recrystallization time depends on the amorphous spot size, and crystal growth velocities can be as high as 50 m/s (1 μm diameter melt-quenched, amorphous laser spot recrystallizing in 10 ns).[79] For nucleation-dominated material, the laser exposure leads to the formation of new nuclei in the whole laser spot area and crystallization occurs by nucleation and growth. The recrystallization time does not depend on the amorphous spot size, and crystal growth velocity cannot easily be deduced. In all these experiments, there is no control over the temperature, which varies in both time and location. The shortest recrystallization times were of the order of 400 ps for 1 μm spot diameters,[80] leading to averaged crystal growth velocities over 1000 m/s for Sb alloys with a small Ge fraction.

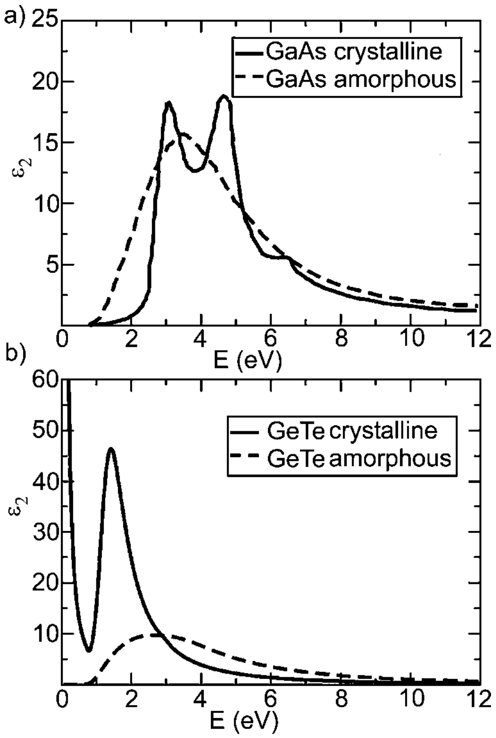

Figure 15. Experimental optical absorption of GaAs (a) and GeTe (b) in the crystalline and amorphous phase. Compared to the changes in GeTe, the differences between the two spectra in GaAs are small. No valence-4 alloy such as GaAs or Si has been reported to be suitable for phase-change applications.

5. Optical Properties of Phase Change Materials

As mentioned in the second section, historically the electrical switching in phase change materials had been discovered and described before the potential of these materials for optical data storage was recognized. Employing a chalcogenide material containing Si, Ge, As, and Te, Ovshinsky[5] found a reversible transition between a highly resistive and a conductive state. The switching was performed by the application of an electrical pulse.[5] Subsequently, however, commercial and scientific interest focused mainly on the change of *optical* properties in phase change materials.[81] In common tetrahedral semiconductors such as Si, Ge, or the III−V compound GaAs, a moderate change in optical properties is found upon amorphization. This is shown in Figure 15a, which displays the imaginary part of the dielectric function of crystalline and amorphous GaAs. The changes between the two phases are rather subtle. The curve for the amorphous phase is higher for small energies and more smeared out compared to the curve for the crystalline phase. These differences are explained by a smearing of the electronic density of states resulting from the loss of long-range order and the formation of defect states in the optical gap of the amorphous state.[82] However, for phase change materials such as GeTe, these changes are much more pronounced. In Figure 15b, the same comparison is shown for amorphous and crystalline GeTe. Three major differences can be observed: a Drude peak present in the crystalline phase but absent in the amorphous one, a blue shift of the amorphous curve, and a strong decrease of the peak intensity in the amorphous phase. This decrease of intensity is of particular importance for the application in optical data storage, as it ensures two different read-out signals for the two phases. It has been observed in several chalcogenide compounds. Studying alloys along the GeTe−Sb_2Te_3 pseudobinary line, Yamada et al.[83] found a rapid phase transition from the crystalline to the amorphous state accompanied by a significant change in reflectivity. They reported that thin films of such compounds, sandwiched between ZnS layers, can be amorphized and recrystallized by laser irradiation. Upon crystallization, the complex index of refraction changed from 4.7 + i1.3 to 6.9 + i2.6 in $Ge_1Sb_2Te_4$ and from 5.0 + i1.3 to 6.5 + i3.5 in $Ge_2Sb_2Te_5$ with 830 nm laser radiation. The crystalline structure of the films has been identified as fcc-like with Te atoms occupying one sublattice while Ge, Sb, and vacancies occupy the other sublattice. On the other hand, it is known that the stable ground state structure of these materials is a layered hexagonal phase made of alternating blocks of GeTe and Sb_2Te_3 (see e.g. ref 21, 26, and 84). Hence, the switching takes place between the metastable crystalline phase observed only in thin films and the amorphous phase. Another phase change material successfully employed for optical data storage is the quaternary alloy Ag−In−Sb−Te or AIST (e.g., the composition $Ag_{3.4}In_{3.7}Sb_{76.4}Te_{16.5}$).[85] Like the Ge−Sb−Te alloys, it is switched between a metastable fcc phase and the amorphous phase. Furthermore, the phase transition in these alloys is accompanied by a relatively large density change of 5−10%,[59,86] which has been suggested to be closely linked to the large optical contrast. Recently, this idea has been stated more precisely after revealing that local structural changes occur upon amorphization. The changes of electronic properties have been studied based on the observed changes in the local atomic structure upon amorphization, first reported by Kolobov et al.[54,55] Using *ab initio* methods, it has been found that a change from octahedral to tetrahedral short-range order results in significant changes of the electronic properties around the Fermi energy. It results in an opening of the electronic band gap and a decrease of Te-p states upon amorphization.[87]

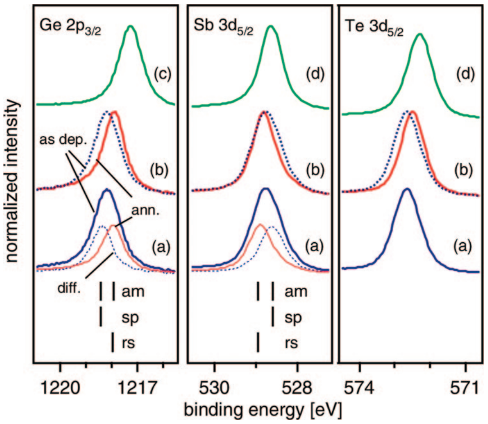

Figure 16. Deep core-level spectra of $GeSb_2Te_4$ deposited at room temperature [full blue lines in (a) and dotted blue line in (b)] and after annealing [solid red line in (b)]. At the top, reference spectra from an amorphous Ge film (c) and from a crystalline Sb_2Te_3 film (d) are included. The Ge and Sb spectra of the as-deposited amorphous (am) $GeSb_2Te_4$ film can be deconvoluted into two components, which are identified with different local environments. Reprinted with permission from ref 88. Copyright 2008 by the American Physical Society.

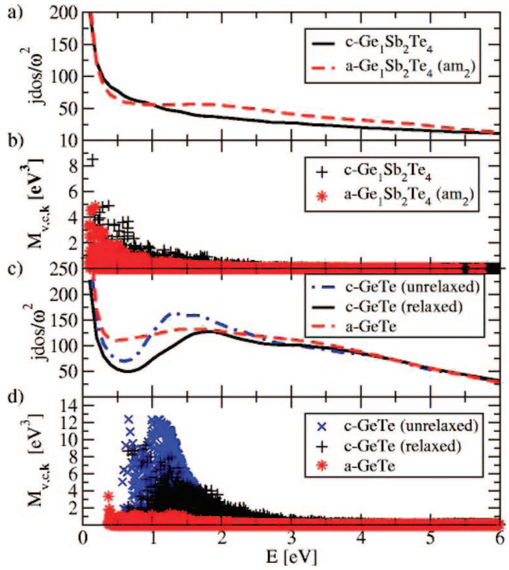

Figure 17. (a) JDOS/ω^2 of $Ge_1Sb_2Te_4$ in the crystalline (c) and the amorphous (a) states in number of transitions/eV^3 per cell and *k*-point. Up to 1.4 eV, the JDOS in the crystalline phase is stronger than that in the amorphous state, while ε_2 is stronger in the crystalline phase up to 1.8 eV. For GeTe (c) up to 1.7 eV, more transitions are found in the a-state compared to the relaxed c-phase. For both materials, the decrease in the absorption upon amorphization can only be explained by taking into account the velocity matrix elements shown in (b) ($Ge_1Sb_2Te_4$) and (d) (GeTe). Reprinted with permission from ref 89. Copyright 2007 by the American Physical Society.

Moreover, Klein et al.[88] found that the core level spectra of the Ge 2p and 3d states as well as those of the Sb 3d states shift upon amorphization. The spectra in the amorphous phase can only be explained if two different local environments are present around the Ge and Sb atoms (see Figure 16). This finding is consistent with the predicted coexistence of 4-fold and 6-fold coordinated Ge in the amorphous state. Employing first principle calculations, it has been found that such a structural rearrangement not only changes the electronic density of states but moreover also results in significant changes of the optical properties. The results of this study are surprising: The optical contrast between the two phases is not due to changes in the electronic density of states as mentioned above for GaAs but rather to the transition matrix elements, i.e. the oscillator strength of the optical transitions. The matrix elements decrease significantly when the local order changes from octahedral to tetrahedral, as observed in many phase change materials. Figure 17, presenting the joint density of states (JDOS) with

$$\mathrm{JDOS}/\omega^2 \equiv \frac{1}{N_k \omega^2} \sum_{v,c,k} \delta(\varepsilon_{c,k} - \varepsilon_{v,k} - \omega) \qquad (19)$$

and the velocity (**v**) matrix elements of the optical transitions **m** with

$$\mathbf{m}_{v,c,k} \equiv \langle c|\mathbf{v}|v\rangle \qquad (20)$$

or the corresponding absolute squared value *M*

$$M_{v,c,k} = 2\frac{4\pi^2}{\Omega}\lim_{q\to 0}\frac{1}{q^2}|\mathbf{m}_{v,c,k}|^2 \qquad (21)$$

illustrates these findings. Here c, v, ε_c, and ε_v are the eigenstates and eigenenergies, respectively, ω is the frequency of excitation, Ω is the volume of the cell, and N_k is the number of k points. Hence, the change in local order and the resulting decrease of the oscillator strength in the amorphous phase are identified as the origin of the large optical contrast in phase change materials.[89]

Furthermore, it has been found that the optical properties in the metastable crystalline phase are strongly influenced by the concentration of vacancies in the system. As described in the section on structural properties, the rock-salt phase of Ge−Sb−Te alloys features a vacancy concentration unknown in other semiconductors. In $Ge_1Sb_2Te_4$ it amounts to 25% on the Ge/Sb-sublattice. Studying Ge−Sb−Te alloys with vacancy concentrations on the Ge/Sb-sublattice ranging from 0% to 25%, an intriguing correlation between vacancy concentration, distortions, and optical properties has been found. Reducing the number of vacancies leads to less local distortions. A broadening of the Ge−Te and Sb−Te partial pair correlation function is observed in the vacancy-rich alloys, denoting a less well-defined nearest-neighbor distance and thus a distortion of the bonds. The degree of the distortions, however, is directly coupled to the optical absorption. It decreases with an increasing degree of distortions in the crystalline phase.[23] As the formation energies of these vacancy-rich systems are relatively low (<0.5 eV), it is possible to tune the vacancy concentration over a wide range and thus modify the optical properties in the crystalline state. Hence, the optical contrast between the crystalline and the amorphous phases, which is fundamental for optical data storage technology, can be optimized by changing the stoichiometry and systematically reducing the number of vacancies. This theoretical prediction has been verified experimentally for the alloys $Ge_xSb_2Te_4$ and $Ge_2Sb_xTe_4$ with $1 < x < 2$ (Figure 18). Thus, these microscopic models provide a basis for a systematic design of material properties in phase change materials, which so far have been based on empirical methods instead. A successful example of such an empirical approach is given by a combination of experiments and calculations from first principles: it has been demonstrated that only alloys which crystallize in a rock-salt lattice show a sufficiently large optical contrast.[90,91] Recently, a more general argument has been provided to distinguish phase change materials from alloys which do not display typical phase change properties. Shportko et al.[17] demonstrated that all phase change materials exhibit resonance bonding in the crystalline phase, while the bonding in the amorphous phase corresponds to ordinary covalent bonding, as found in typical III−V semiconductors. Further studies have shown that only specific stoichiometric combinations show resonant bonding.[92] Based on this work, alloys suitable for application as phase change materials can be identified from the position of the constituent elements in the periodic table.

6. Electrical Properties of Phase Change Materials

6.1. Band Diagram for Chalcogenide Semiconductors

The electrical properties of phase change materials and the understanding of the threshold switching effect are crucial for the application of these materials in solid state memory devices. This section will first discuss the semiconductor band diagrams for chalcogenide semiconductors in the crystalline and the amorphous phases. After briefly describing the electrical properties of the crystalline phase, we will focus on electrical phenomena in the amorphous phase, including transport, threshold switching, and transient delay effects.

Figure 19 schematically shows band diagrams for a chalcogenide semiconductor in either the crystalline (a) or the amorphous phase (b).[93,94] There are three important differences between the two diagrams: First, most generally the energy gap for the amorphous phase is large compared to the crystalline phase. For instance, optical absorption and photoconductivity data indicate that the gap of amorphous $Ge_2Sb_2Te_5$ is about 0.7 eV, whereas the crystalline phase has an energy gap of about 0.5 eV.[95,96] Second, while the

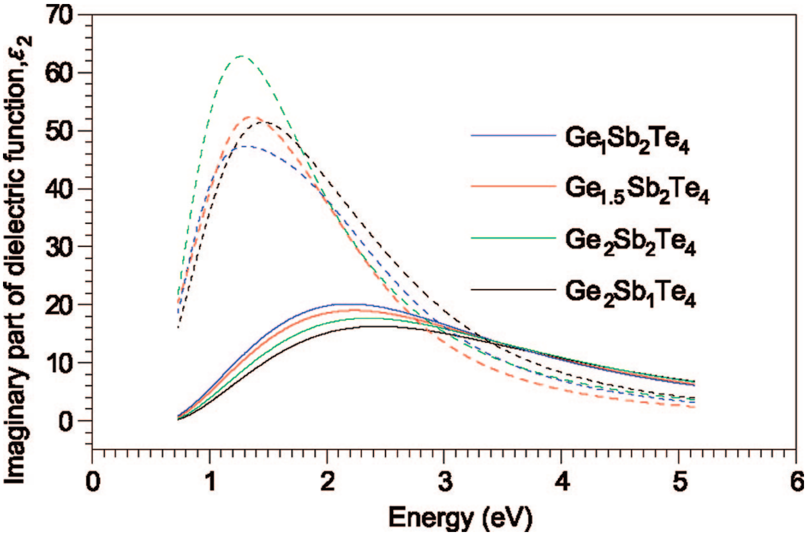

Figure 18. Imaginary part of the dielectric function for the amorphous (solid lines) and crystalline phases (broken lines) of the $Ge_1Sb_2Te_4$−$Ge_2Sb_2Te_4$ alloys and of $Ge_2Sb_1Te_4$. There is a systematic increase in absorption with decreasing Ge and Sb vacancy concentrations which is consistent with the theoretical predictions. Reprinted by permission from Macmillan Publishers Ltd.: Nature Nanotechnology[23] (Copyright 2007).

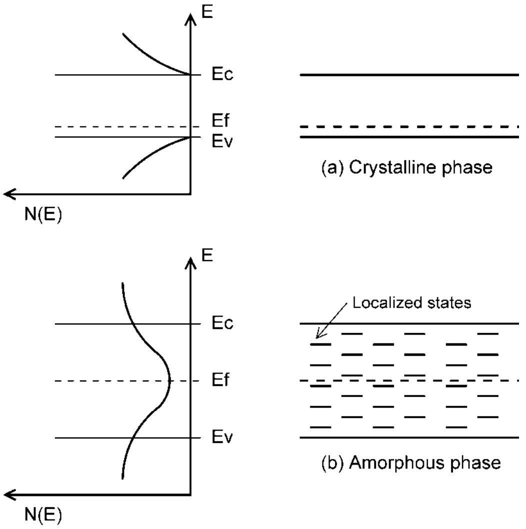

Figure 19. Schematic drawing of the band diagrams for a chalcogenide semiconductor in either the crystalline (a) or the amorphous (b) phase. Reprinted with permission from ref 94. Copyright 2008 IEEE.

forbidden gap and conduction/valence bands are clearly distinct in the crystalline phase, the amorphous phase is characterized by a large concentration of localized states in the gap.[97] These localized states significantly contribute to the density of states: Thus, the strong difference between gap and conduction/valence bands is not in the presence/absence of available states, as for the crystalline phase, but rather in their *localization*, or equivalently the mobility of carriers occupying the states. Deep states tend to be highly localized, while mobility increases for energies approaching the conduction or valence bands. For this reason, the energy gap in an amorphous semiconductor is generally referred to as a *mobility gap*, namely an energy range with insufficient mobility of states, rather than a forbidden range with no states, as in standard crystalline semiconductors.

The third difference regards the position of the Fermi level: due to the large concentration of localized states, the Fermi level is pinned at about midgap in the amorphous chalcogenide.[93] For this reason, the electrical resistivity and the respective activation energy E_A are relatively large. For instance, activation energies around 0.25−0.35 eV have been observed in amorphous $Ge_2Sb_2Te_5$.[98] On the other hand, the crystalline chalcogenides generally display a small activation energy for conduction, which is compatible with a self-doping behavior, probably due to point defects (e.g., vacancies) in some Te compounds.[23]

6.2. Electrical Conduction in the Crystalline Phase

The crystalline phase, at least for a classical phase-change material such as $Ge_2Sb_2Te_5$, appears as a relatively low band gap, doped semiconductor, for which the standard semiconductor theory can be straightforwardly applied. The typical approach to describe electrical conduction in the crystalline phase is the drift-diffusion equation.[99,100] This results in a typically ohmic behavior for relatively low applied voltage, as shown by the measured $I-V$ (current−voltage) curves in Figure 20.[101] Also, the measured E_A is relatively low, as shown by the Arrhenius plot of resistance for the set state (corresponding to the crystalline phase) in Figure 21, giving a value of about 20 meV for E_A.[102] On the contrary, the reset state (corresponding to the amorphous phase) displays large resistance and activation energy (Figure 21), consistently with the band diagram in Figure 19.

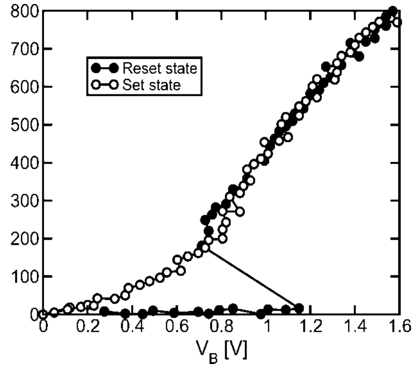

Figure 20. Measured $I-V$ curves for a PCM cell in the set (open symbols) or reset (filled symbols) states. The latter displays the threshold switching effect at about $V_T = 1.2$ V. Reprinted with permission from ref 101. Copyright 2007 IEEE.

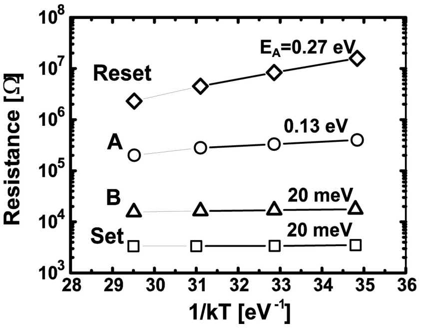

Figure 21. Arrhenius plots of the resistance for a fully reset state, a fully set state, and two incomplete set states, A and B, obtained by the application of a voltage pulse to a phase change memory cell in the initial reset state. Reprinted with permission from ref 102. Copyright 2004 IEEE.

The $I-V$ curve for the crystalline phase displays a nonlinear behavior for relatively large voltage in Figure 20. To explain this feature, we may recall that measurements in the figure were obtained for μTrench (named for its geometric design; see also section 8.2) phase change memory cells, where electrical conduction and heating were strongly confined for the purpose of low-current phase change in the memory cell.[103] As a result, a current of a few 100 μA may result in significant heating (a few hundred kelvin), thus causing significant thermal carrier generation in the low-band gap semiconductor. The increase of carrier density results in a conductivity increase with voltage, responsible for the nonlinear $I-V$ curve in Figure 20.

An important aspect from the perspective of a phase change memory operation is electrical conduction in *intermediate* states, which display resistance values between the set and reset values and consist of a mixed amorphous−crystalline phase. To study the electrical properties of intermediate states, Figure 21 shows the Arrhenius plot for two incomplete set states, obtained by the application of a voltage pulse to a phase change memory cell in the initial reset state. The current during the applied pulse results in a significant Joule heating and a consequent crystallization of the amorphous phase. Crystallization can be described by nucleation and growth effects (see section 4), resulting in a fine mixture of crystalline grains embedded in the amorphous network. Electrical conduction in this mixed-phase volume can be explained by percolation of carriers through dispersed

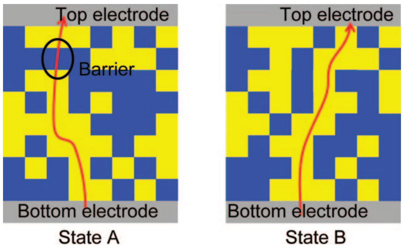

State A

State B

Figure 22. Schematic drawing of two different mixed-phase configurations, characterized by an incomplete (A) or complete (B) percolation path through low-resistivity crystalline grains. In state A, the electrical current is limited by a small amorphous "barrier" whereas no amorphous barrier exists for state B. Yellow, crystalline; blue, amorphous.

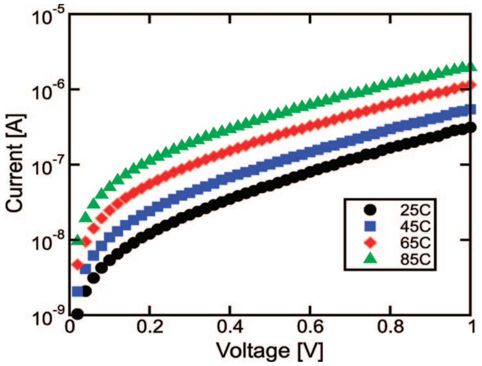

Figure 23. Measured $I-V$ characteristics in the subthreshold regime for amorphous $Ge_2Sb_2Te_5$ at increasing temperature. Reprinted with permission from ref 106. Copyright 2007 American Institute of Physics.

low-resistivity crystalline grains.[104,105] This is schematically shown in Figure 22 for two different mixed-phase states, characterized by an incomplete (A) or complete (B) percolation path through low-resistivity crystalline grains. In state A, the electrical current is limited by a small amorphous "barrier", thus accounting for the relatively large values of resistance and activation energy (0.13 eV) in Figure 21. No amorphous barrier exists for state B; thus, the activation energy is the same as that of the bulk crystalline phase (full set state). However, the resistance still remains higher than the set state due to geometrical effects, namely a small cross section and a relatively large percolation length through the mixed phase.

6.3. Electrical Conduction in the Amorphous Phase

Figure 23 shows the measured $I-V$ curves for a phase change memory cell in the reset state at variable temperature.[106] The reported current range is below 2 μA, which cannot be resolved in the linear-current plot of Figure 20. According to the standard interpretation, conduction is due to Poole−Frenkel (PF) conduction; namely, electrons at localized states are thermally emitted into free states in the conduction band, where they can freely move.[93] Recently, it was noted that not only pure thermal emission above the conduction band edge but also thermally activated tunneling below the conduction band contribute significantly to conduction.[107] The combined transport due to thermally activated PF and tunneling accounts for the strong temperature dependence of the current in the figure. To gain more insight into this conduction mechanism, it is convenient to extract the activation energy for conductivity, reporting the measured current in an Arrhenius plot for variable voltage. This is shown in Figure 24 for values of the applied voltage V = 0.4, 0.7, and 1 V.[98] The activation energy, which can be obtained as the slope of data in the Arrhenius plot, decreases for increasing voltage, which is consistent with the PF model. In fact, as described in Figure 25, the energy barrier between two localized states, equal to $\Delta\phi(0)$ for zero applied voltage (a), is lowered to a value $\Delta\phi(V)$ by the application of a voltage (b). Thus, the activation energy for the conduction process, which is equal to the potential barrier $\Delta\phi(V)$, decreases with V as shown in Figure 24.

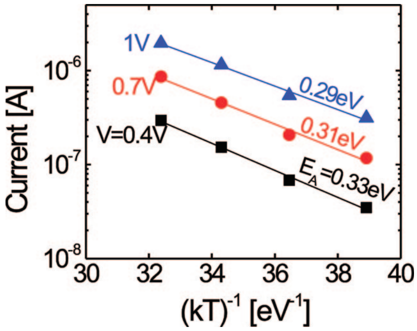

Figure 24. Arrhenius plot of the measured current for increasing voltage $V = 0.4$, 0.7, and 1 V (right). Reprinted with permission from ref 98. Copyright 2007 American Institute of Physics.

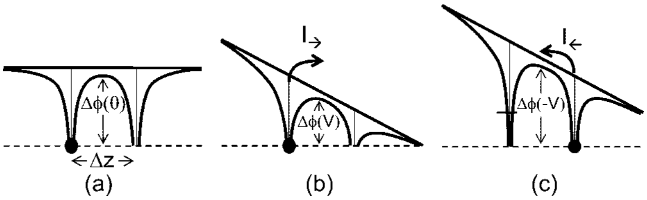

(a)

(b)

(c)

Figure 25. Schematic for the analytical model for subthreshold transport. The current is due to electrons being emitted from one trapped state to another, over a potential barrier. The potential barrier is equal to $\Delta\phi(0)$ when no voltage is applied (a), and it drops to $\Delta\phi(V)$ as a voltage V is applied, resulting in an exponential enhancement of the forward current $I_\rightarrow$ (b). The reverse contribution to the current $I_\leftarrow$ is exponentially lowered by the increase of the potential barrier $\Delta\phi(-V)$ (c). Reprinted with permission from ref 98. Copyright 2007 American Institute of Physics.

A simple analytical model for the PF conduction can be obtained from Figure 25. From the figure, the barrier lowering can be approximated to a linear function of V. In fact, if the distance Δz between traps is small compared to the electrostatic Coulomb range and for reasonably low fields, the energy barrier $\Delta\phi(V)$, corresponding to the potential maximum between the two wells, can be approximated as the barrier value at halfway between the two traps, namely:

$$\Delta\phi(V) = \Delta\phi(0) - qF\frac{\Delta z}{2} = E'_C - E_{F0} - qV\frac{\Delta z}{2u_a} \tag{22}$$

where F is the electric field between the two traps, E'_C is the conduction-band mobility edge, E_{F0} is the equilibrium Fermi level, and u_a is the total thickness of the amorphous chalcogenide layer where the voltage V is applied.[106] The mobility edge E'_C is used instead of the proper conduction band edge to take into account the tunneling contribution.[107] The current in the forward direction $dI_\rightarrow$, corresponding to electrons at localized states between E and $E + dE$, can thus be written as

$$
\begin{aligned}
\mathrm{d}I_{\rightarrow} &= qA_{\mathrm{a}}n_{\mathrm{T}}(E)\mathrm{e}^{-\Delta\phi(V)/kT}\frac{\Delta z}{\tau_0}\,\mathrm{d}E \\
&= qA_{\mathrm{a}}N_{\mathrm{T}}(E)\exp\left(-\frac{E'_{\mathrm{C}}-E_{\mathrm{F0}}}{kT}\right)\frac{\Delta z}{\tau_0}\,\mathrm{d}E\ \times \\
&\exp\left(\frac{qV}{kT}\frac{\Delta z}{2u_{\mathrm{a}}}\right)\mathrm{d}E \qquad (23)
\end{aligned}
$$

where q is the electron charge, A_a is the cross section of the amorphous region, n_T [cm^{-3} eV^{-1}] is the density of localized electrons contributing to PF conduction, and τ_0 is an attempt-to-escape time. Equation 22 was used for the potential barrier $\Delta\phi(V)$, while the density of localized electrons was obtained by the Maxwell–Boltzmann statistics as $n_T(E) = N_T(E) \exp(-(E - E_{F0})/kT)$, where N_T [cm^{-3} eV^{-1}] is the trap density. In eq 23, the conduction is assumed to be uniform in the cross section A_a and the average electron velocity is computed as the intertrap spacing Δz divided by the average escape time, given by the attempt-to-escape time τ_0 (typically in the 10^{-13}–10^{-14} s range) divided by the escape probability $P_e = \exp(-\Delta\phi(V)/kT)$. Similarly to eq 23, the reverse current $I_{\leftarrow}$ can be obtained as

$$
\mathrm{d}I_{\leftarrow} = qA_{\mathrm{a}}N_{\mathrm{T}}(E)\exp\left(-\frac{E'_{\mathrm{C}}-E_{\mathrm{F0}}}{kT}\right)\frac{\Delta z}{\tau_0}\exp\left(-\frac{qV}{kT}\frac{\Delta z}{2u_{\mathrm{a}}}\right)\mathrm{d}E \qquad (24)
$$

where the minus sign in the second exponential factor signifies a barrier increase for electrons heading in the direction opposite to the electrostatic force. The net current I can thus be obtained as the integral of the contributions $\mathrm{d}I_{\rightarrow} + \mathrm{d}I_{\leftarrow}$, thus leading to

$$
I = 2qA_{\mathrm{a}}N_{\mathrm{TOT}}\exp\left(-\frac{E'_{\mathrm{C}}-E_{\mathrm{F0}}}{kT}\right)\frac{\Delta z}{\tau_0}\sinh\left(\frac{qV}{kT}\frac{\Delta z}{2u_{\mathrm{a}}}\right) \qquad (25)
$$

where N_{TOT} [cm^{-3}] is the density of states integrated in the energy range from E_{F0} to E'_C. Similarly to eq 25, the contribution due to trapped holes can be derived and added to calculate the whole PF current.

Equation 25 can account for the shape of the measured $I-V$ curves shown in Figure 23. In particular, the sinh-like voltage dependence accounts for the ohmic behavior of the current at very low voltages (approximately below 0.2 V) and for the exponential increase of the current for relatively high voltages.

From eq 25, a closed-form expression for the activation energy can be obtained deriving the logarithm of the current versus $1/kT$, thus yielding

$$
E_{\mathrm{A}} = -\frac{\mathrm{d}\log I}{\mathrm{d}(1/kT)} = E'_{\mathrm{C}} - E_{\mathrm{F0}} - qV\frac{\Delta z}{2u_{\mathrm{a}}}\coth\left(\frac{qV}{kT}\frac{\Delta z}{2u_{\mathrm{a}}}\right) \qquad (26)
$$

which, for sufficiently large voltage, can be linearly approximated as $E'_C - E_{F0} - qV\Delta z/2u_a$. Figure 26 shows measured and calculated activation energies as a function of voltage, obtained from the $I-V$ characteristics at variable temperature in Figure 23. The analytical expression in eq 26 can account for both the linear decrease of E_A with voltage at sufficiently large voltage and for the saturation at low voltage. The decrease of E_A with voltage is consistent with data in Figure 24 and is due to the lowering of the potential barrier between two trapped states for increasing voltage. The activation energy saturates to $E'_C - E_{F0} - kT$ in the ohmic regime, due to the competition between forward and reverse conduction.[106]

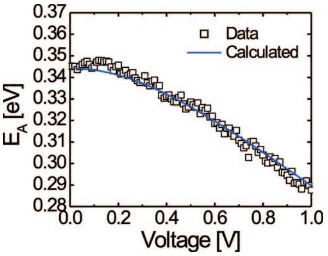

Figure 26. Activation energy E_A, as a function of voltage, obtained from experimental $I-V$ curves at variable temperature, and simulation results from the full analytical expression for E_A, from eq 26. Reprinted with permission from ref 106. Copyright 2007 American Institute of Physics.

The voltage-dependent E_A for transport is a strong evidence for the PF transport model in Figure 25. However, the nature of the positively charged defects acting as trapping centers is still not completely clear. These states may correspond to already present ionized donor states, which become neutral at the capture of one electron.[108] The concentration of donor states can be estimated by the ratio $\Delta z/u_a$ obtained from the subthreshold slope (Figure 23 and eq 24) or the voltage-dependence of E_A (Figure 26 and eq 26). From these data and from the estimated thickness of the amorphous layer u_a of about 30 nm from TEM observations, the donor-trap concentration is found to be in the range of a few 10^{18} cm^{-3}. The number of such donor states is rather low, if compared to the defect-annihilation dynamics accompanying the structural relaxation (SR) of the amorphous chalcogenide, revealed by the steady increase of resistivity.[94,109] The smooth increase of reset-state resistance during SR would indicate a concentration of localized states larger than a few 10^{19} cm^{-3}. This discrepancy may be explained assuming that donor states are only a minority of the (mostly neutral) localized states.[110] Electrons traveling by PF transport through the neutral sites are still affected by the potential landscape due to donor states, thus accounting for the potential barrier lowering in Figure 25. Alternatively, the local positive charge accounting for the trapping potential may result from the self-trapping, or polaron, effect:[93,111,112] Trapping of an electron may induce a local polarization, resulting in the buildup of a local positive charge. According to this explanation, the measured activation energy for electron transport also includes the energy required for the local structural rearrangement to accommodate the electron, and not only the potential barrier between the trapped level around E_{F0} and the conduction band edge E'_C.[107]

6.4. Threshold Switching in the Amorphous Phase

The most peculiar feature in the electrical characteristics of amorphous chalcogenide is the so-called *threshold switching* effect.[5] If the phase change material is in the highly resistive amorphous phase and a certain electrical field is applied to the material, it will suddenly (within nanoseconds) become highly conductive. This process does not necessarily lead to a phase change; it is reversible if the current pulse is so short that it does not heat the material above the crystallization temperature for long enough time to cause

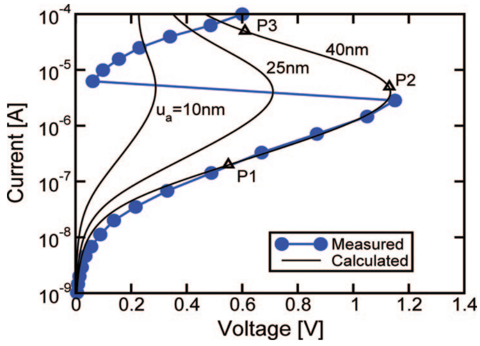

Figure 27. Measured *I*−*V* curve for a phase-change memory cell with amorphous $Ge_2Sb_2Te_5$ chalcogenide and calculation results obtained from solution of eq 34 for three values of the amorphous chalcogenide thickness, namely u_a = 10, 25, and 40 nm. Reprinted with permission from ref 107. Copyright 2008 American Physical Society.

crystallization. Threshold switching is clearly visible in Figure 20, where the *I*−*V* curve displays a voltage snap-back from the threshold voltage V_T at about 1.15 V. Similarly, Figure 27 shows a typical *I*−*V* curve in a logarithmic current scale, displaying the subthreshold regime and the snap-back at approximately constant current. Threshold switching is the result of a negative-differential-resistance (NDR) behavior: Increasing the voltage in the subthreshold region, an unstable point (V_T) is reached, corresponding to the transition from a positive differential resistance (the subthreshold regime) to the NDR region. In a real experiment, the current suddenly jumps to the next available stable positive-differential-resistance state, that is the ON state (about 200 μA in Figure 20). In the ON state, the current is typically so large that the amorphous chalcogenide is quickly crystallized: for this reason, the measured *I*−*V* curve above the threshold switching point generally corresponds to a crystallized chalcogenide phase.

To explain the NDR at the basis of threshold switching, several different physical models have been proposed. Among these models, we may mention thermal instabilities,[113] impact ionization and Shockley−Hall−Read recombination,[95,114] polaron instabilities,[112] and crystallization.[115] Most recently, NDR was explained by PF transport at high electric fields, causing an increase of the average energy of carriers.[107] Energy-gain effects in the PF conduction at high fields were first proposed by Jonscher to account for high-frequency hopping conduction in amorphous semiconductors.[118] As schematically shown in Figure 28a, electrons at relatively low fields obey the equilibrium conduction model at the basis of eq 25, i.e. a Fermi statistics where approximately all the states below (above) E_{F0} are filled (unfilled) by electrons. On the other hand, at relatively high electric fields (Figure 28b), electrons can gain energy from the applied field, resulting in an off-equilibrium energy distribution with higher occupation probability at high energy levels. Due to the exponential energy dependence of the escape time in eq 23, even a small increase of energy, e.g. in the range of few *kT*, can result in a huge enhancement of conductivity, thus resulting in significant instability of conduction.

The energy gain effects can be simply described by introducing the concept of *quasi Fermi energy* E_F, that is the energy for which the electron occupation probability is $^1/_2$. Since the current is mainly due to carriers lying around the Fermi level, E_F can also be viewed as the average energy of electrons mostly contributing to the current. This description is equivalent to considering the effect on the electron temperature,[106] which increases under an applied electric field similarly to the hot-carrier effect in crystalline semiconductors.[117] To estimate the quasi Fermi energy E_F as a function of the applied electric field, we consider the simple schematic in Figure 29, representing the energy balance in a thin slice d*z* along the direction of the current in the amorphous region.

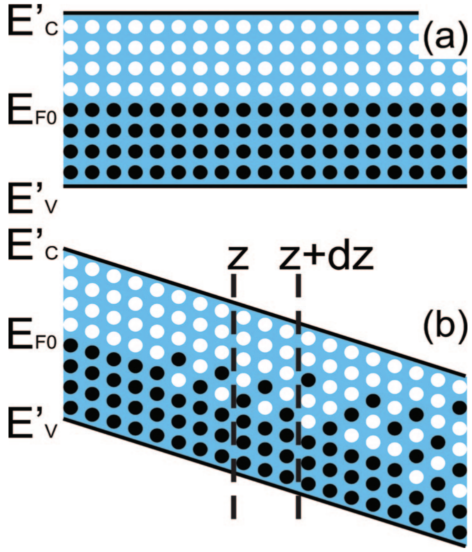

Figure 28. (a) Schematic for the energy distribution of electrons in the amorphous chalcogenide film at equilibrium (no applied electrical field). The mobility edges at the conduction and valence bands E′C and *E*′V, respectively, and the Fermi level E_{F0} are shown. Black and white circles schematically represent occupied and unoccupied localized states. (b) is the same as (a) but under off-equilibrium conditions at high electric field. Note the increase in average energy E_F. Reprinted with permission from ref 107 (2008), by the American Physical Society.

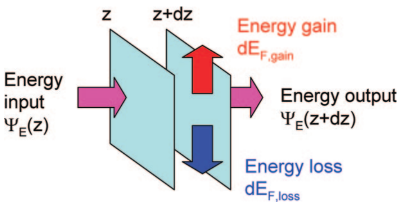

Figure 29. Schematic representing the energy balance in a thin slice d*z* along the direction of the current in the amorphous region. The balance between energy input $\Psi_E(z)$ and energy output $\Psi_E(z + dz)$ is given by the energy gain $dE_{F,gain}$ due to the field and the energy gain $dE_{F,loss}$ due to relaxation within the slice.

The input flow of energy $\Psi_E(z)$ [J cm^{-2} s^{-1}] associated with electrons entering the slice at *z* is given by

$$\Psi_E(z) = \frac{J(z)\,E_F(z)}{q} \tag{27}$$

whereas the output flow of energy $\Psi_E(z + dz)$ [J cm^{-2}s^{-1}] due to electrons exiting the slice at *z* + d*z* is similarly given by

$$\Psi_E(z + dz) = \frac{J(z + dz)\,E_F(z + dz)}{q} \tag{28}$$

where *J* is the hopping current density. The energy gain $dE_{F,gain}$ [J] in the slice due to the electric field is given by[118]

$$dE_{F,gain} = qF(z)\,dz \tag{29}$$

while the rate of energy loss $\mathrm{d}E_F/\mathrm{d}t_{\text{ loss}}$ [J s^{1-}] associated with relaxation phenomena can be written as

$$\left.\frac{\mathrm{d}E_F}{\mathrm{d}t}\right|_{\text{loss}} = -\frac{E_F - E_{F0}}{\tau_{\text{rel}}} \tag{30}$$

where τ_{rel} is a relaxation time. The energy loss is proportional to the average excess energy, as usual in the description of hot carriers[117] and as already proposed by Jonscher for hopping electrons in disordered semiconductors.[110] The relaxation time τ_{rel} describes the interaction between electrons and phonons. The energy loss $\mathrm{d}E_{F,\text{loss}}$ [J] can be obtained by dividing the rate in eq 30 by the average electron velocity, thus yielding

$$\mathrm{d}E_{F,\text{loss}} = \left.\frac{\mathrm{d}E_F}{\mathrm{d}t}\right|_{\text{loss}} \frac{qn_{\text{TOT}}}{J(z)}\mathrm{d}z \tag{31}$$

where the concentration n_{TOT} [cm^{-3}] of trapped electrons contributing to the current has been used. The concentration can be calculated as

$$n_{\text{TOT}} = N_{\text{TOT}}\frac{kT}{E'_C - E_{F0}} \tag{32}$$

namely assuming that electrons occupy only a range kT of the trap density N_{TOT} [cm^{-3}].[93] The energy balance of Figure 29 thus reads

$$\begin{aligned} &\frac{J(z + \mathrm{d}z)\, E_F(z + \mathrm{d}z)}{q} - \frac{J(z)\, E_F(z)}{q} \\ &\quad = \frac{J(z)}{q}(E_{F,\text{gain}} - E_{F,\text{loss}}) \\ &\quad = J(z)\, F(z)\, \mathrm{d}z - \frac{E_F - E_{F0}}{\tau_{\text{rel}}} n_{\text{TOT}}(z)\, \mathrm{d}z \end{aligned} \tag{33}$$

After some elaboration, and noting that continuity requires $J(z) = J(z + \mathrm{d}z)$, we obtain the differential equation[107]

$$\frac{\mathrm{d}E_F}{\mathrm{d}z} = qF - \frac{qn_{\text{TOT}}}{J}\frac{E_F - E_{F0}}{\tau_{\text{rel}}} \tag{34}$$

Equation 34 can be solved with the analytical model in eq 25 corrected by the replacement of E_{F0} by E_F, and with the basic relationship between electrostatic potential and electric field:

$$F = \frac{\mathrm{d}E'_C}{q\, \mathrm{d}z} \tag{35}$$

$I-V$ curves calculated with the model in eq 34 are shown in Figure 27 for three different thicknesses of the amorphous layer, namely $u_a = 10$, 25, and 40 nm. The calculated curve for $u_a = 40$ nm best accounts for the experimental $I-V$ characteristics in both the subthreshold region and the switching point. Calculations predict the NDR at the basis of threshold switching, with a threshold voltage of about 1.1 V. Note again that the $I-V$ curve above the switching point corresponds to the crystalline phase, as a result of the long time spent in the high current regime during the $I-V$ measurement. Thus, experimental and calculated results should be compared limitedly to the subthreshold/threshold regimes.

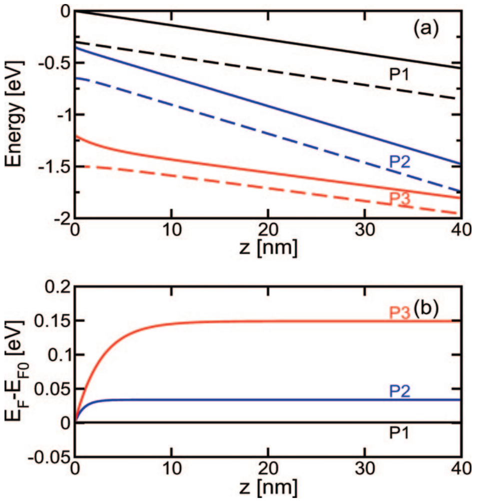

Figure 30. Calculated profiles of conduction-band mobility edge E'_C [solid line, (a)], quasi-Fermi level E_F [dashed line, (a)], and average excess energy $E_F - E_{F0}$ (b), for the three bias points P1, P2, and P3 in Figure 27. The thickness of the amorphous chalcogenide layer is $u_a = 40$ nm.

To understand the physical origin for the NDR in Figure 27, Figure 30 shows the calculated profiles for E'_C, E_F (a), and the *average excess energy* $E_F - E_{F0}$ (b) as a function of the position along the amorphous layer z, obtained from the solution of eq 34. Three bias points are considered, representing the subthreshold region (P1), the threshold point (P2), and the ON state in the NDR region (P3, also shown in Figure 27). In the subthreshold bias point P1, the excess energy is almost negligible, since the electric field is still insufficient to originate substantial energy gain. Correspondingly, the field profile is flat and the potential profile E'_C is almost linear. At the threshold-switching point P2, the energy increases far from the cathode up to a value of about kT, which corresponds to an increase of current density J at constant field by a factor e. Since the current must remain continuous at steady state and since there is no conductivity enhancement close to the injection electrode, a redistribution of the electric field is necessary, thus resulting in a nonlinear potential profile. At even higher current levels, in the ON state P3, $E_F - E_{F0}$ further increases to about 150 meV, thus causing a large nonuniformity of the field and a stronger bending of E'_C. The relatively large excess energy strongly enhances conductivity, thus allowing us to sustain a large current with a relatively small voltage drop across the amorphous layer. This results in a significant voltage with respect to the threshold switching point. Therefore, the keys to understand NDR according to this model are (i) the energy gain due to the high electric field in the proximity of the negative electrode and (ii) the consequent low voltage drop in the so-called ON region.

From a device-design perspective, it is important to clarify what is the critical condition for threshold switching. As already mentioned, threshold switching (i.e., the transition from subthreshold to NDR regimes) occurs when an energy increase of about kT is reached. This condition can be rephrased in terms of the electrical power density P_T''' for switching, given by the formula:[107]

$$P_T''' = JF = \frac{\gamma_T N_{TOT}(kT)^2}{\tau_{rel}(E'_C - E_{F0})} \qquad (36)$$

Equation 36 predicts that (i) the product of switching current and voltage is a constant for constant temperature and amorphous volume, and (ii) the switching power increases with the square of temperature for constant amorphous volume. It is useful to note that, due to the relationship between electric field and current density from eq 25, the constant power condition can be translated in equivalent constant electric field, which was previously observed in the literature.[119]

6.5. Delay Time for Threshold Switching

While the previous section focuses on the modeling of threshold switching within a steady-state approach, it is important to consider the most general case of a *transient* switching phenomenon, where switching occurs after some time from the application of the voltage. A transient theory of switching may allow for important predictions and considerations on the device perspective: First, it can allow for the explanation and prediction of unwanted switching at relatively low voltage during the read operation in the subthreshold regime. Second, it can describe the real case of programming in a memory device, where triangular or rectangular pulses are applied to an amorphous semiconductor device: In such a case, the determination of the minimum delay time for the onset of threshold switching and of the switching time for the completion of the transition from the low to the high conductivity state is critical for the performance evaluation.[120]

Figure 31 shows the cumulative distribution of measured delay times for a PCM device.[120] In each measurement, the device was programmed by a fixed reset pulse and then a second read pulse at a voltage close to the switching point was applied after a fixed *sleep* time of 1 ms from the reset pulse. The constant reset voltage ensured that the volume of chalcogenide material transformed into the amorphous phase remained constant, while the constant sleep time allowed for the same structural relaxation effect after the initial quenching of the liquid phase into a metastable amorphous phase.[101] The delay time τ_D was determined as the time from the application of the read voltage to the switching event observed during the read pulse. The read voltage was varied within a relatively small range to detect the voltage dependence of τ_D. The experimental results in the figure indicate that (i) τ_D strongly decreases for increasing applied voltage, and (ii) the statistical spread of τ_D is about constant and extremely large. As a figure of merit of the statistical spread, the distributions were plotted in a Weibull scale, and the shape factor β, that is the slope of the distributions in the Weibull diagram, was evaluated. The Weibull scale was chosen in analogy with the time-dependent dielectric breakdown in dielectrics, most typically silicon dioxide, for which the delay time obeys a Weibull distribution with generally large shape factor $\beta > 1$.[121] In the case of τ_D, β was always found to be below one.

The observed strong voltage dependence and the large statistical spread of τ_D can be explained by the transient switching model depicted in Figure 32. During the read pulse, the amorphous chalcogenide is biased at a constant voltage below threshold, where the current is fluctuating due to $1/f$ noise (f is the frequency).[122,123] Flicker noise is generally observed in semiconductors displaying PF conduction, due to the stochastic nature of the trapping/emission processes at the basis of the transport phenomenon.[123] Due to these fluctuations, the current can eventually exceed the threshold condition, resulting in a switching event. A condition of constant switching current I_T was assumed for simplicity: In fact, the constant switching power condition in eq 36 can be to a good approximation assumed to correspond to constant current if the voltage is only marginally changed during the experiments. This physical picture was verified by a Monte Carlo numerical model, able to simulate stochastic $1/f$ noise fluctuations of the current and to determine the τ_D as the time for the earliest event of a fluctuation exceeding I_T.[120]

Figure 33 shows the measured and calculated delay time τ_D (a) and its respective Weibull shape factor β (b) as a function of applied voltage V_A. In both cases, the Monte Carlo simulations account reasonably for the data. The exponential dependence in Figure 33a is extremely steep (about 13 mV per decade of τ_D) and can be explained by (i) the exponential increase of the current in the subthreshold regime (Figure 32) and (ii) the Gaussian distribution of the current amplitude in the time domain, both resulting in a strong increase of the switching probability as the bias point approaches the nominal threshold switching point. The calculated shape factor in Figure 33b is in the range between 0.6 and 0.7 for the considered range of voltages, in good agreement with experimental observations. For comparison, Monte Carlo simulations of white (instead of $1/f$) noise, where the power spectral density is constant as a

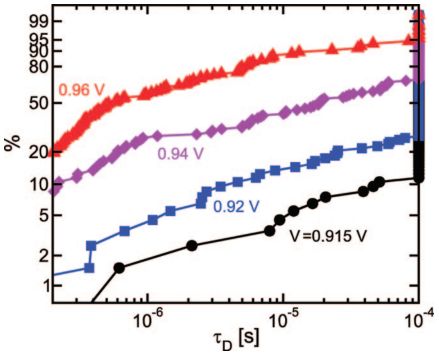

Figure 31. Cumulative distribution of measured delay times τ_D for a phase change memory device. The device was programmed by a fixed reset pulse, and then a second read pulse was applied after a fixed *sleep* time of 1 ms. The delay time τ_D was determined as the time from the application of the read voltage to the switching event observed during the read pulse. Reprinted with permission from ref 120. Copyright 2008 IEEE.

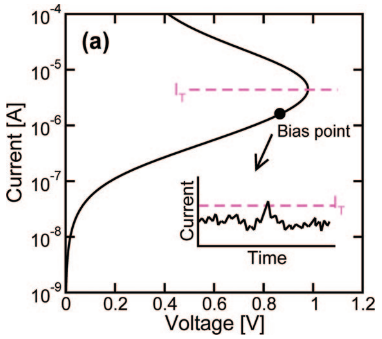

Figure 32. Schematic for the transient switching model. During the read pulse, the amorphous chalcogenide is biased at a constant voltage below the threshold current I_T. Fluctuation of the bias current (inset) due to $1/f$ noise eventually results in threshold switching. Reprinted with permission from ref 120. Copyright 2008 IEEE.

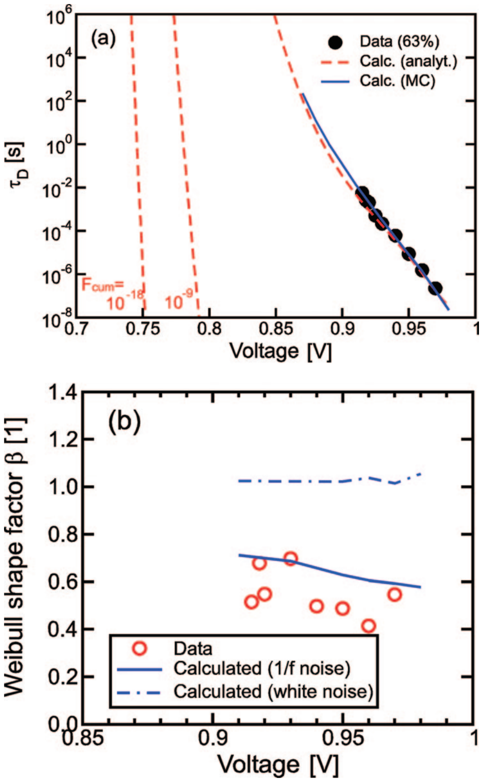

Figure 33. Measured and calculated delay time τ_D (a) and its respective Weibull shape factor β (b) as a function of the applied voltage V. Reprinted with permission from ref 120. Copyright 2008 IEEE.

function of frequency, display a larger shape factor of about 1. The low shape factor of τ_D is due to the strong role of low-frequency fluctuations characterizing $1/f$ noise: A large-amplitude, low-frequency component can, in fact, considerably accelerate or delay the switching, depending on its phase.[120]

The Monte Carlo model can straightforwardly allow for read-disturb extrapolations, aimed at the calculation of the delay time for switching within a large array for variable voltage. The extrapolations were done with the use of an analytical model for transient switching, replacing the Monte Carlo model to allow for relatively fast calculations of long delay times at low bias, and assuming a conservative value of the Weibull shape factor of 0.6. Results shown in Figure 33a indicate a very low probability F_{cum} of read disturb even at relatively large read bias around 0.7 V. It should be noted, however, that such extrapolations only take into account the intrinsic delay time due to $1/f$ noise fluctuation in the amorphous semiconductor, while other important possible sources of read disturb are not considered, e.g. (i) voltage fluctuations of nonideal bias circuits and (ii) nonideal distributions of threshold voltage and subthreshold characteristics in the memory array, due to statistical spread of the reset current and of the material composition.[124]

7. Scaling Properties of Phase Change Materials

The application of phase change materials in technological devices leads to the study of scaling properties of these materials because it is essential to know how materials properties change as mark size and film thickness (for optical recording) or memory cell dimensions shrink. In particular, those material parameters that are important for the specific application are investigated.

For optical recording, the following parameters need to be studied as a function of film thickness and mark (bit) size: (1) crystallization speed, (2) melt-quenching (amorphization) speed, determined among other parameters by the (3) melting temperature, (4) thermal stability of the amorphous phase, and the related (5) crystallization temperature, (6) optical constants, and (7) thermal conductivity. For phase change memory cells, some of these parameters are irrelevant, e.g. optical constants, but some are as important, such as crystallization speed, melting temperature, thermal stability of the amorphous phase, and thermal conductivity. Additional electrical parameters need to be investigated, including the (8) resistivities in both phases and the (9) threshold voltage as a function of film thickness or device size. At some point, materials will cease to be phase change materials where the ultimate limit might be the number of atoms to form a crystalline unit cell, so the (10) size at which phase change does not occur anymore is an important parameter to know.

(1) The crystallization time of a given material can vary as a function of substrate and capping layer,[125] and this influence becomes stronger as film thickness is reduced because the interfaces play a more and more important role. As was discussed in the section on switching kinetics, heterogeneous nucleation typically dominates the nucleation process, and with reduced film thickness, this becomes even more pronounced. Crystallization times of as-deposited phase change materials are often measured by static laser testers, but it has been shown that they can be orders of magnitude different from recrystallization times.[79] In a typical recrystallization experiment in either optical discs or memory devices, an interface between the amorphous and crystalline phases exists from which the crystals can grow; therefore, nucleation is not required. The difference in crystallization times is particularly large for materials with low nucleation rates but high crystal growth rates, such as Ag−In−Sb−Te or Ge−Sb materials. For technological applications, only recrystallization times are relevant.

Recrystallization times as a function of film thickness were measured by determining the so-called complete erasure time (CET) of an amorphous mark in a crystalline matrix for optical discs.[126–128] Opposite behavior was observed by Zhu comparing growth-dominated (Ag−In−Sb−Te) and nucleation-dominated (Ge−Sb−Te) materials with a decrease for growth-dominated and an increase for nucleation dominated materials as film thickness was reduced.[127,129] Since short CETs are favorable to increase data transfer, growth-dominated materials might be better suited for discs with very thin films. Very thin films are required for multilayer discs for which the films need to be transparent to some degree. However, Martens et al.[126] observed that there is a minimum in CET at 9 nm film thickness for Sb−Te based materials, and for thinner film thickness, the CET increased again. The thinnest film of the Ag−In−Sb−Te material measured by Zhu was close to this minimum, so he might not have observed it because he did not measure very thin films. The introduction of crystallization-promoting interfacial layers such as SiC reduced CETs up to a factor of 2,[127,128] demonstrating the strong effect of interfaces.

Recrystallization in memory devices was studied as a function of device diameter[129] using $Ge_2Sb_2Te_5$ as the storage material. While materials similar to this composition showed increased CET with reduced film thickness, $Ge_2Sb_2Te_5$ showed shorter crystallization times with reduced device diameter. Figure 34 shows that the shortest switching times

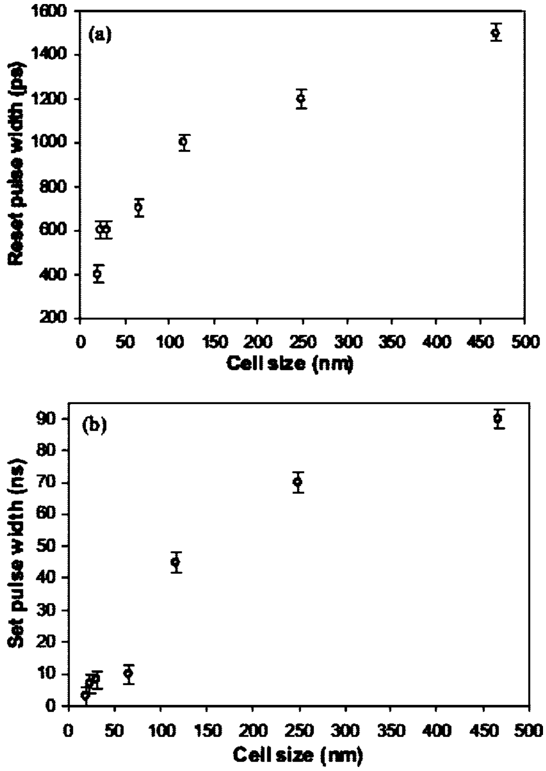

Figure 34. Shortest switching pulse width as a function of cell size varying from 500 to 19 nm for (a) set and (b) reset measured on pore devices. The pulse amplitudes are 0.8 V for set and 4.5 V for reset. Reprinted with permission from ref 129. Copyright 2008 American Institute of Physics.

were 2.5 ns for set (recrystallization) and 400 ps for reset (reamorphization) operations for a 19 nm diameter pore cell.

$Ge_2Sb_2Te_5$ nanowire devices behaved similarly.[130] They were fabricated by contacting nanowires of different diameters between 20 and 190 nm grown by the vapor−liquid−solid method. The nanowires are crystalline as grown and were amorphized by short current pulses. Their recrystallization times were found to be about 2 orders of magnitude shorter for the smaller devices.[130] It is clear from these results that geometries and interfaces play very important roles for ultrascaled devices. From a memory device perspective, the scaling behavior is favorable because switching times are reduced.

(2) The amorphization time is determined by the time it requires to heat the material above its melting temperature, which in turn is determined by the melting temperature itself, the available power, and the thermal environment. Very fast melting times of 1 ps have been reported using fast laser testing on Sb films with 6 atomic % Ge,[131] and melting times were found to be shorter for thinner Sb films.[132] Fast optical heating is easier to achieve than fast Joule heating caused by electrical current pulses because inherent capacitances limit pulse rise times to hundreds of picoseconds. As mentioned above, the fastest reported reamorphization of a memory cell was 400 ps (Figure 34a).[129]

(3) The melting temperature of phase change materials as a function of size has been studied for thin films,[133] nanowires,[134] and nanoparticles.[135] The studies are very limited but show in all cases a reduction of melting temperature as dimensions are reduced. Time-resolved X-ray diffraction (XRD) of GeTe films was performed during heating.[133] It showed that the crystallization temperature as indicated by the appearance of diffraction peaks was increased while the melting temperature as indicated by the disappearance of the peaks films was reduced as film thickness was reduced. The thinnest films that showed still diffraction peaks were 2 nm, and their melting temperature was 600 °C, more than 100 °C lower than that of bulk GeTe (725 °C). The melting temperature of thinner films cannot be detected by this method, since they do not crystallize anymore.

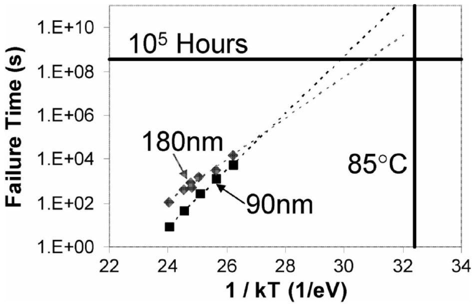

Figure 35. Comparison of cell-level data retention between 180 and 90 nm devices. Reprinted with permission from ref 138. Copyright 2007 IEEE.

For phase change nanowires, a strong reduction in melting temperature was observed.[134] GeTe nanowires with diameters between 40 and 80 nm were grown by the vapor−liquid−solid method, and their melting temperature was measured by heating *in situ* in a TEM. Melting was observed for temperatures as low as 390 °C (compared to 725 °C for bulk GeTe). Because these measurements were performed in ultrahigh vacuum, the melting temperatures cannot directly be compared to measurements at atmospheric pressure such as the XRD experiments.

Data on the melting temperature of phase change nanoparticles are very sparse. Milliron[135] reported on a reduction of the melting point of GeTe nanoparticles that were fabricated by solution-based chemistry.[136,137] Aliquots were taken after different reaction times corresponding to particles of different size. The particle size distribution was quite broad, but it can be assumed that shorter time aliquots had smaller particles than longer time aliquots. Reduction in the melting temperature to 590 °C for smaller particles and to 620 °C for larger particles was observed using time-resolved XRD.

Reduced melting temperatures are technologically favorable, since they lead to reduced power requirements for switching.

(4) The thermal stability of the amorphous phase as a function of size was studied on phase change memory devices fabricated with 180 and 90 nm lithography technologies and $Ge_2Sb_2Te_5$ material.[138] Cells were reset into the amorphous state and time to failure (drop in resistance) was measured at elevated temperature. The devices fabricated with 90 nm technology failed at slightly shorter times than the larger devices, indicating a reduced stability of the amorphous phase at smaller dimensions (Figure 35). Similarly, experiments on the recrystallization of amorphized nanowires[130] showed faster recrystallization, remarkable several orders of magnitude higher nucleation rates, and activation energies that were inversely proportional to the device diameter, falling from 2.34 eV for 190 nm devices to 1.9 eV for 19 nm devices. These effects were explained by fast heterogeneous nucleation at the wire surface with an increased role as the surface/volume ratio is increased.

This scaling behavior needs to be of concern because it leads to reduced data retention. One practical way to solve

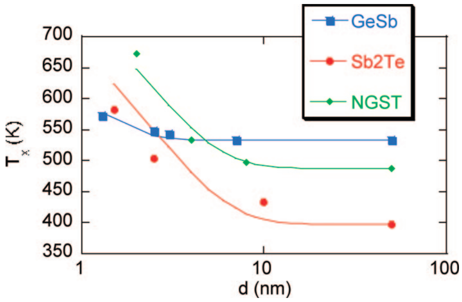

Figure 36. Crystallization temperature T_x as a function of film thickness for various phase change materials: GeSb, Sb with 15 atomic % Ge; NGST, nitrogen-doped $Ge_2Sb_2Te_5$. Reprinted with permission from ref 141. Copyright 2008 American Institute of Physics.

this problem is to use phase change materials with higher crystallization temperature, which is correlated to higher activation energy.[139]

(5) The crystallization temperature is one of the most important parameters of phase change materials, and it is a function of size. For thin films of $Ge_2Sb_2Te_5$,[140] nitrogen-doped $Ge_2Sb_2Te_5$, Ge−Sb with 15 atomic % Ge, Sb_2Te, and Ag- and In-doped Sb_2Te,[141] crystallization temperatures were measured as a function of film thickness using the drop in resistivity connected with the phase change[140] or time-resolved XRD during heating.[141] It was found that crystallization temperatures increase for films thinner than 10−15 nm, as shown in Figure 36 for different phase change materials and for oxide substrates and capping layers. This is only the case for certain substrates and capping materials. In another study, it was shown that the crystallization temperature of Ge−Sb with 15 atomic % Ge can increase or decrease with reduced film thickness depending on the cladding material and can differ by almost 200 °C for the thinnest films of 3 nm.[142] This demonstrates the increasing influence of interfaces on the crystallization behavior of thin films as film thickness is reduced and the importance of heterogeneous nucleation. The reduction of the crystallization temperature was found for metal cladding materials and might be connected to metal-induced crystallization. More research is needed to clarify the role of metal-induced crystallization (which is established for other amorphous semiconductors such as Si)[143] for phase change materials. The strong increase of the crystallization temperature for thin films between oxides[140−142] is in stark contrast to the decrease in crystallization temperature of nanowires as they shrink in diameter,[130] and it is not clear where this difference originates from. The nanowires are typically covered by a thin GeOx layer formed by their exposure to air after the deposition.[134] Nanoparticles with sizes above about 20 nm have crystallization temperatures that are comparable to bulk material, but smaller nanoparticles have been found to have higher crystallization temperatures in most cases,[144−147] with the exception of nanoparticles made from spin-on Ge−Sb−Se phase change material, which had about 30 °C lower crystallization temperature than thick films made from the same material.[148]

Increased crystallization temperatures are technologically favorable because they lead to better data retention, as mentioned above. The increase in required switching power is not a drawback because the melt-quench (reset) operation needs the highest power, not the crystallization (set) operation.

(6) The optical constants of phase change materials also change with film thickness. Miao et al.[149] determined the optical constants *n* and *k* using ellipsometry in the wavelength range between 400 and 800 nm for $Ge_1Sb_2Te_4$ and found increased optical constants for thinner films, in particular at smaller wavelengths. Stronger light absorption, in particular at smaller wavelength (the operating wavelength for the latest generation optical discs such as Blu-ray discs), is favorable because for very thin films the optical contrast is reduced, since the films are almost transparent.

(7) The thermal conductivity as a function of film thickness was measured by Reifenberg et al.[150] using nanosecond laser heating and thermal reflectance measurements on Ge−Sb−Te films with thicknesses between 60 and 350 nm. They found a substantial decrease in thermal conductivity for both the amorphous and crystalline phases as film thickness was reduced. Reduced thermal conductivity is desirable to reduce heat losses in memory devices.

(8) The resistivity as a function of film thickness does not change very much. Wei et al.[140] observed a small increase in the resistivity of the amorphous phase for the thinnest $Ge_2Sb_2Te_5$ films between 3.5 and 10 nm. This hardly influences the on/off ratio of several orders of magnitude between the amorphous and crystalline phases.

(9) The threshold voltage is a function of device dimensions because the threshold condition is met when a threshold electric field is applied (as was described in detail in the section about the threshold switching), which translates into a certain voltage depending on the geometry of the devices. Threshold fields have been reported for doped SbTe (14 V/μm,[151] 8 V/μm)[152] and Ge−Sb with 15 atomic % Ge (9 V/μm).[153] In today's phase change memory devices, typical threshold voltages are in the 1 V range because a typical switching volume is about 50−100 nm thick along the dimension of the applied voltage. Typical reading voltages are around 50 mV. When dimensions shrink, the threshold voltage will too.[106,107] On the other hand, the cell resistance will increase and higher reading voltages are required to obtain sufficient detectable reading current signal.[99,100] There is a certain operating window for which the reading voltage is well below the threshold voltage that depends on the resistance of both phases and the threshold field of a given material. This window shifts with device dimensions and depends on the material.

(10) The size at which phase change does not occur anymore is the ultimate scaling limit. Gotoh et al.[154] produced small crystalline marks in amorphous $Ge_2Sb_2Te_5$ films using an atomic force microscope (AFM). They observed that the smallest marks they could produce were about 10 nm, but they had a very short lifetime of a few minutes. Nanoscale amorphous marks in a crystalline film were also demonstrated by AFM and scanning tunneling microscopy (STM), and the smallest sizes were 10 and 100 nm, respectively.[155] Using conventional AFM[156] or AFM equipped with a nanoheater,[157] storage densities of 1−3.3 Tb/inch^2 could be achieved. These high storage densities are supported by theoretical work[158] that shows that, under optimized film thickness, capping layer, and substrate conditions, stable amorphous marks in a crystalline film or crystalline marks in an amorphous film with diameters in the range of 10−30 nm can be written by an electrical probe.

The thinnest blanket films that still showed crystallization as detected by XRD were found to be 1.3−2 nm depending on the material.[141] Figure 37 shows as an example the intensity of diffracted X-ray peaks as a function of temperature for a 50 nm and a 1.3 nm thick Ge−Sb film with 15

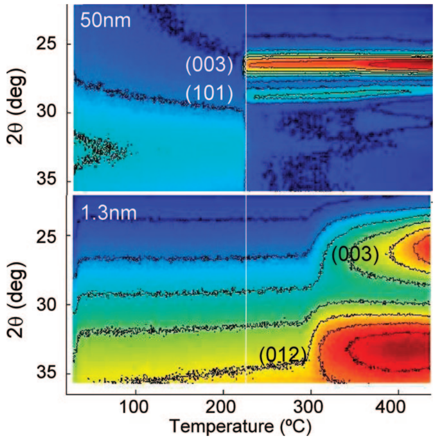

Figure 37. Time-resolved XRD peak intensity for 50 nm (top) and 1.3 nm (bottom) thick films of Sb with 15 atomic % Ge. Reprinted with permission from ref 141. Copyright 2008 American Institute of Physics.

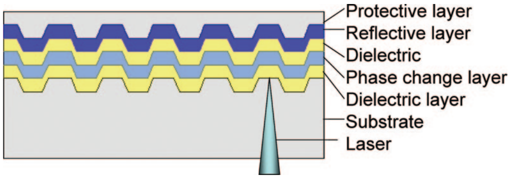

Figure 38. Schematic of a single-layer rewritable DVD.

atomic % Ge. One can see that the as deposited films are amorphous (no XRD peaks). The thick film crystallizes at around 235 °C, as indicated by the appearance of XRD peaks. The indexed peaks belong to Sb, and there is a very weak Ge(111) peak at around 32° that appears at higher temperature around 350 °C. The thin film crystallizes at higher temperature, at around 350 °C. The peaks are much broader because the film is so thin and grains are very small, but they are clearly visible. The phase transition occurs over a wider temperature range.

$Ge_2Sb_2Te_5$ films as thin as 3.5 nm showed crystallization as measured by a drop in resistivity.[140] Phase change nanoparticles produced by solution-based chemistry can be as small as 2−5 nm and are single crystalline.[135,136] It appears that the limit for crystallization is in the very few nanometer range; this is very promising for technological applications.

8. Applications of Phase Change Materials

8.1. Optical Data Storage Based on Phase Change Materials

Rewritable optical storage media apply the difference in reflectivity between the amorphous and the crystalline phases to store information. The discs are multilayer structures (Figure 38) sputter deposited on a crenellated substrate.[159] The phase change material is sandwiched between two dielectric layers, typically ZnS-SiO_2. This material was selected because it has a large refractive index, high melting point, very small grains, low thermal conductivity, and low internal stress. A reflective layer increases the amount of energy absorbed in the phase change film, and an additional protective layer prevents the disc structure from mechanical damage. Recording is performed in most cases only in the grooves for better track isolation. As mentioned earlier, as deposited, amorphous phase change materials crystallize at very different rates (typically slower) than melt-quenched, amorphous materials. To ensure good performance, discs are "initialized", which means crystallized, and recording is done by writing amorphous bits into a crystalline matrix.

Three generations of rewritable optical storage media have been developed: rewritable compact discs (CDs), digital versatile discs (DVDs), and Blu-ray discs, with ever increasing storage capacity from 500 MB of early CDs (1990) to 50 GB of today's dual layer Blu-ray discs. Some typical parameters for current products are as follows: data transfer rates of 36 Mbps, recording track pitch of 320 nm, data bit length of about 100−120 nm, and numerical aperture of 0.85.[159] Two classes of phase change materials have been applied in optical discs: materials on the GeTe-Sb_2Te_3 pseudobinary line and around Sb_2Te doped with a few atomic % of In and Ag.[15]

A main driving force for research in new materials has been the decrease of the wavelength of the laser used for writing, reading, and erasing bits. By decreasing the wavelength, the size of the written bits decreases as well and, hence, the storage density increases. For CDs the wavelength is 780 nm, for DVDs 650 nm are used, and for Blu-ray discs 405 nm are employed.[15] While the alloy $Ge_2Sb_2Te_5$ possesses a high optical contrast in the red and infrared spectral range and was therefore used in CDs and DVDs, alloys with larger Ge content such as $Ge_8Sb_2Te_{11}$ have a higher optical contrast in the blue spectral range and are used for Blu-ray discs.[160] A further decrease of the laser wavelength beyond visible blue light is very challenging, as light emitting diodes are not available for this spectral range. Hence, the next generation of optical storage media will require a different approach.[161] A technology based on near-field optics using a so-called solid immersion lens (SIL)[162,163] has been proposed by Philips. The SIL hovers only 30 nm above the disc and increases the numerical aperture from 0.85 for the standard Blu-ray technology to 1.9. As the high aperture increases spatial resolution, bits of smaller sizes can be read and written, moving beyond the diffraction limit in air.[164] Another technology takes advantage of the so-called Super-RENS (Super-resolution near-field structure) effect.[165−168] Here an optically nonlinear layer, e.g. Sb, is deposited on top of the recording layer. The interaction with the laser turns this additional layer into a mask for the laser which allows for writing and reading in the optical near field of the phase change layer. Similar to the SIL, this effect allows for reading and writing structures below the wavelength of the laser. The origin of this effect, however, is not yet fully understood. In order to allow for rewritable data storage, phase change materials will play an important role for both the SIL as well as the Super-RENS based technology.

8.2. Phase Change Random Access Memory

PCRAM technology is based on the electrical switching of small volumes of phase change materials repeatedly between the amorphous and the crystalline phases. A relatively large and short current pulse is applied to a memory cell that heats the material by Joule heating above its melting point, which is around 600 °C for a typical material used in PCRAM (Figure 1, top). The short trailing edge of the current pulse leads to fast cooling of the molten material, and it is quenched in the amorphous phase. After such operation (reset), the cell is in the high resistive state. A longer and lower current pulse is applied to switch it back to the crystalline, low resistive state (Figure 1, bottom). When the pulse is applied, first the current flow is very small because

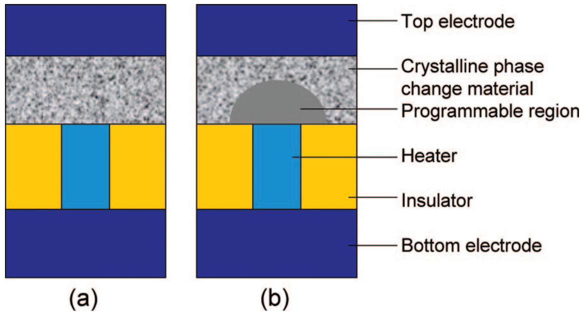

Figure 39. Schematic of a mushroom cell.

the cell is in the high resistive state. When the applied voltage surpasses the threshold voltage (see section on electrical properties), the cell becomes suddenly very conducting, and a large current flows and heats the phase change material by Joule heating. The current pulse needs to be long enough so that the material is above its crystallization temperature for a time sufficiently long for crystallization. This time will depend on the cell design and the phase change material. Small current pulses are used to read the state of the device, and they need to be small enough so that they do not introduce any phase change. A typical $I-V$ characteristic is shown in Figure 20.

The most common cell design is the so-called mushroom cell, owing its name to the shape of the switched volume. Figure 39 shows a schematic of a mushroom cell: Figure 39a in the set state; Figure 39b in the reset state. In the set state, the entire phase change material is crystalline; in the reset state a mushroom-shaped area on top of the heater is amorphous. This area needs to have a larger diameter than the heater at the heater interface for a complete reset so that amorphous material is fully blocking the current path. The fraction of phase change material that does not switch is in the crystalline phase because the back-end-of-the-line CMOS (complementary metal-oxide-semiconductor) processes used to manufacture the cells include a bake at 400 °C for 30 min. This temperature is above the crystallization temperature of any technologically applied phase change material.

High programming currents were the reason why early devices were not commercialized,[169] and also for today's devices the reduction of the programming current is of great importance. Every memory cell is controlled by an access device which delivers the current pulses and which in most cases is a transistor (diodes have been reported also).[170] Currently the required reset currents determine the size of these access devices, which are much larger than the actual memory cell and determine the data storage density. Therefore, reset current reduction is paramount, and many new cell designs have been proposed and realized for this reason.

Reset current reduction can be achieved by reducing the amount of material that needs to be switched or by better confining the heat or both.[100] Modifications of the mushroom cell include a ring bottom electrode to reduce the contact area.[171] Other cell designs, such as the edge contact cell[172] and the μTrench cell,[173] achieve reduced reset current also by reduced contact area whereas the pore cell[174] and the pillar cell[175] achieve reset current reduction by confining the switching volume. Planar devices, such as the line[151] and bridge devices,[176] have also been fabricated. Overviews on PCRAM cell design, characteristics, and technological process integration can be found in refs 177–179.

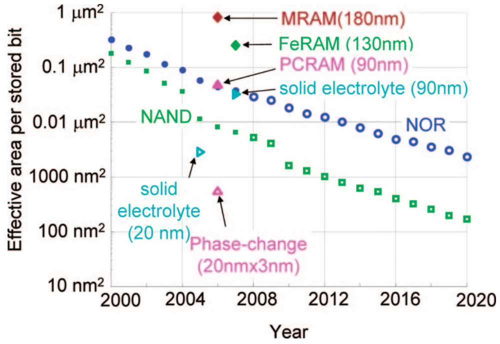

Figure 40. Effective area per stored bit for NAND and NOR Flash as a function of year. Also shown (full symbols) are recent demonstrations of fully integrated memory arrays for various storage class memory candidates and single-device demonstrations. Reprinted with permission from ref 183. Copyright 2008 IBM.

8.3. Future Applications of Phase Change Materials

The development of PCRAM technology opens up the opportunity to look into future applications. The first market PCRAM technology will move into is probably the niche market of radiation-hard memory for spacecraft, since BAE has announced plans for production of a 4-Mbit chip for this year.[3] One of the most successful memory technologies today is Flash memory. It generated $23 billion in worldwide revenue in 2007,[180] and the Flash memory industry today drives semiconductor equipment manufacturers to develop next generation tools to enter the sub-50-nm lithography regime. Both NOR and NAND Flash (referring to the different circuit architectures and being optimized for fast program code execution or low cost memory, respectively)[180] are very successful technologies, with prices of $10 per gigabyte for NAND Flash in 2007, and will be so in the near future. Flash memory based drives are now on the market that will probably replace hard disk drives in the next decade because of their increasingly low costs and higher reliability.[181]

A more likely application of PCRAM is in the field of so-called storage-class memory.[182] Storage-class memory will be a solid-state based technology combining high performance and reliability with low cost and archival capability.[183] Flash can be considered a possible storage class memory, but there are other contenders such as ferroelectric RAM (FeRAM), magnetic RAM (MRAM), resistive (oxide based) RAM, organic and polymeric memory, solid-electrolyte based memory, and PCRAM. Scalability and cost will mainly decide which technology will dominate the storage class memory area, but PCRAM is a strong candidate, in particular if programming currents (power consumption) can be reduced by scaling.[183] Figure 40 shows the excellent scaling capabilities of PCRAM compared to other technologies.

Dynamic RAM (DRAM) consists of one transistor and one capacitor and stores information as charge in the capacitor. Since the capacitor is leaky, DRAM is volatile and needs frequent refreshing, but it is rather fast (15−25 ns cycle time for standalone DRAM, 1.5 ns for embedded DRAM) and delivers very high cycle numbers ($10^{15}-10^{17}$). As mentioned above, very fast PCRAM switching has been demonstrated with crystallization in 2 ns and melt-quenching in 400 ps using very small pore-type devices (see Figure 34).[129] The very high cycle numbers still need to be demonstrated: 10^{13} cycles have been reported on relatively large devices.[184] Some aspects of the circuit design are based on the fact that DRAM is volatile and needs frequent refreshing of the data, and a nonvolatile DRAM-replacement would enable conceptually different chip designs.

Future applications for PCRAM might include field-programmable gate arrays or reconfigurable logic[185] where the phase change materials function as programmable wires or can perform summing operations. Even more far out applications are concerned with cognitive computing. PCRAM devices can be set into multilevel resistance states,[186] which is an interesting feature for cognitive computing concepts. Ovshinsky proposed to apply PCRAM to develop cognitive computers[187–189] because many functions that are required for cognitive computing can potentially be fulfilled by a PCRAM cell. These functions include, for example, what neuroscientists call plasticity of synapses and what engineers would call different resistance states of a cell depending on the values and timing of the inputs they receive. Another function is the potential ability to perform cell switching after a certain number of input pulses have been received sequentially or simultaneously.[190] The potential to build nanoscale devices that can emulate the functions of neurons or synapses[191] would be a very important first step to build computers that function similarly to a brain.

9. Summary/Outlook

Phase change materials possess a unique combination of properties. They exhibit large differences in physical properties such as reflectivity and electrical resistivity between the amorphous and crystalline phases which are due to structural differences between the phases. The structural differences can be attributed to significant differences in the bonding for these states. Phase change materials can also be switched fast and repeatedly between those two phases. The most successful phase change materials are characterized by a simple cubic structure with atoms on random locations in the lattice, often with large numbers of vacancies and distortions. This enables these materials to crystallize rapidly. Another specific feature of phase change materials, the existence of the threshold-switching, is required for PCRAM technology. This effect allows for the presence of two separate memory voltage regimes, for reading and programming, respectively below and above the threshold voltage.

Since its conception in the 1960s, phase change technology has come a long way. At early stages, Te-based alloys were mainly studied which did not possess the required crystallization speed to use them in a viable technology. The discovery of fast-switching materials enabled the development of a whole new technology—phase change based optical rewritable storage. Extensive efforts were focused on a better understanding of the switching mechanisms of phase change materials in order to develop and optimize the storage materials. For optical discs, media were required that exhibit large optical contrast and fast switching at shorter and shorter wavelength to increase storage density, faster switching to increase data rate, and better stability to increase cycle number and archival lifetime.

PCRAM development required a whole new set of optimization parameters to be fulfilled including large electrical contrast, very high cycle numbers, and good data retention at elevated operation temperatures. Many companies work today on the development of PCRAM technology, and the first products are about to enter the market. Most likely in the beginning this will be a niche market such as radiation-hard memory for spacecrafts, but one can envision the replacement of Flash memory or even DRAM. The existence of a nonvolatile DRAM would open the door to radically different, new logic chip architectures. Completely new applications such as phase-change based logic[185] or cognitive computing based on phase change materials are being considered.[187–191]

For the existing and new applications, the material design and optimization are decisive factors. To enable additional and different PCRAM cell designs and fabrication methods, new deposition techniques for phase change materials have been developed. Besides the conventional sputter deposition, other deposition methods such as chemical vapor deposition, atomic layer deposition, electroplating, or spin-on deposition are being explored.[148,192] All these new techniques allow deposition into deep vias or trenches and might lead to new cell architectures that are impossible today because of the very limited via-filling capability of sputter deposition.

Finally, the scalability of phase change technology is of great importance. Extensive research has been performed to study the scaling limits of phase change materials, including work on ultrathin films, nanowires, nanoparticles, and ultrascaled PCRAM devices. The results are very encouraging. It appears that phase change materials do not change their properties dramatically for sizes down to the few nanometers range, and if they do, it is in a way that is favorable for technologies (increased crystallization temperature, reduced melting temperature, faster switching, etc.). They loose their phase change properties around 1−2 nm when essentially not enough atoms are available to form the crystal unit cell.

Phase change materials are the crucial element of the mature rewritable optical storage technology and the emerging PCRAM technology. A better understanding of their properties is paramount to the development of better phase change materials for existing and future technologies.

10. Acknowledgments

S.R. would like to thank Matthew Breitwisch and Bryan Jackson for helpful advice. W.W. acknowledges the Feodor-Lynen-program of the Alexander von Humboldt-Foundation. D.I. gratefully acknowledges funding by Intel.

11. Note Added after ASAP Publication

This paper was published on the Web on August 28, 2009. It was reposted to the Web on January 5, 2010, after corrections were made to eqs 27 and 28.

12. References

(1) Lankhorst, M. H. R. *J. Non-Cryst. Solids* **2002**, *297*, 210.
(2) Yamada, N. In *Phase Change Materials: Science and Applications*; Raoux, S., Wuttig, M., Eds.; Springer: Berlin, Heidelberg, New York, 2008; Chapter 10, pp 199−226.
(3) Rodgers, J.; Maimon, J.; Storey, T.; Lee, D.; Graziano, M.; Rockett, L.; Hunt, K. *Non-Volatile Memory Technology Symposium*; Pacific Grove, CA, 2008.
(4) http://www.itrs.net/Links/2007ITRS/IRCPosition.html.
(5) Ovshinsky, S. R. *Phys. Rev. Lett.* **1968**, *22*, 1450.
(6) Northover, W. R.; Pearson, A. D. U.S. Patent 3,117,013, 1964.

(7) Dewald, J. F.; Northover, W. R.; Pearson, A. D. U.S. Patent 3,241,009. 1966.

(8) Ovshinsky, S. R. U.S. Patent 3,271,591, 1966.

(9) ovonic.com/PDFs/Optical_Memory_Research_Report/History_Of_Phase_Change_Tech.pdf.

(10) Feinleib, J.; deNeufville, J.; Moss, S. C.; Ovshinsky, S. R. *Appl. Phys. Lett.* **1971**, *18*, 254.

(11) Shanks, R. R.; Davis, C. *ISSCC Digest of Technical Papers*; 1978; p 112.

(12) Smith, A. W. *Appl. Opt.* **1974**, *13*, 795.

(13) Yamada, N.; Ohno, E.; Akahira, N.; Nishiuchi, K.; Nagata, K.; Takao, M. *Jpn. J. Appl. Phys.* **1987**, *26* (Suppl. 26-4), 61.

(14) Strand, D.; Tsu, D. V.; Miller, R.; Hennessey, M.; Jablonski, D. *Proc. Eur. Phase Change and Ovonic Sci. Symp.,* Grenoble, France, 2006, available at www.epcos.org.

(15) Yamada, N.; Otaba, M.; Kawahara, K.; Miyagawa, N.; Ohta, H.; Akahira, N.; Matsunaga, T. *Jpn. J. Appl. Phys.* **1998**, *37*, 2104.

(16) Wuttig, M.; Yamada, N. *Nat. Mater.* **2007**, *6*, 824.

(17) Shportko, K.; Kremers, S.; Woda, M.; Lencer, D.; Robertson, J.; Wuttig, M. *Nat. Mater.* **2008**, *7*, 653.

(18) Rabe, K. M.; Joannopoulos, J. D. *Phys. Rev. B* **1987**, *36*, 6631.

(19) Kolobov, A. V.; Tominaga, J.; Fons, P.; Uruga, T. *Appl. Phys. Lett.* **2003**, *82*, 382.

(20) Edwards, A. H.; Pineda, A. C.; Schultz, P. A.; Martin, M. G.; Thompson, A. P.; Hjalmarson, H. P.; Umrigar, C. J. *Phys. Rev. B* **2006**, *73*, 045210.

(21) Matsunaga, T.; Yamada, N. *Phys. Rev. B* **2004**, *69*, 104111.

(22) Sun, Z.; Zhou, J.; Ahuja, R. *Phys. Rev. Lett.* **2006**, *96*, 055507.

(23) Wuttig, M.; Lüsebrink, D.; Wamwangi, D.; Welnic, W.; Gillessen, M.; Dronskowski, R. *Nat. Mater.* **2007**, *6*, 122.

(24) Dronskowski, R; Blöchl, P. *J. Phys. Chem.* **1993**, *97*, 8617.

(25) Kooi, B.; Groot, W.; de Hosson, J. *J. Appl. Phys.* **2004**, *95*, 924.

(26) Agaev, K.; Talybov, A. *Sov. Phys. Crystallogr.* **1966**, *11*, 400.

(27) Karpinsky, O.; Shelimova, L.; Kretova, M.; Fleurial, J. *J. Alloys Compd.* **1998**, *268*, 112.

(28) Friedrich, I. Ph.D. thesis, RWTH Aachen University, Aachen, Germany, 2006

(29) Gaspard, J.-P.; Ceolin, R. *Solid State Commun.* **1992**, *84*, 839.

(30) Robertson, J. *Adv. Phys.* **1983**, *32*, 361.

(31) Burdett, J.; Lee, S. *J. Am. Chem. Soc.* **1985**, *107*, 3063.

(32) Peierls, R. *Quantum theory of solids*; Oxford University Press: 1956.

(33) Tsu, R.; Howard, W. E.; Esaki, L. *Phys. Rev.* **1968**, *172*, 779.

(34) Okoye, C. *J. Phys.:Condens. Matter* **2002**, *14*, 8625.

(35) Bahl, S.; Chopra, K. *J. Appl. Phys.* **1969**, *40*, 4940.

(36) James, A.; Lord, M. *Macmillan's Chemical and Physical Data*; Macmillan: London, U.K., 1992.

(37) Waghmare, U. V.; Spaldin, N. A.; Kandpal, H. C.; Seshadri, R. *Phys. Rev. B* **2003**, *67*, 125111.

(38) He, H.; Thorpe, M. F. *Phys. Rev. Lett.* **1985**, *54*, 2107.

(39) Boolchand, P.; Lucovsky, G.; Thorpe, M. F. *Philos. Mag.* **2005**, *85*, 3823.

(40) Thorpe, M. F.; Jacobs, D. J.; Chubynsky, M. V.; Phillips, J. C. *J. Non-Cryst. Solids* **2000**, *266*, 859.

(41) Phillips, J. *Phys. Rev. Lett.* **2002**, *88*, 216401.

(42) Stevens, M.; Grothaus, J.; Boolchand, P.; Hernandez, J. *Solid State Commun.* **1983**, *47*, 199.

(43) Boolchand, P. *Chalcogenide Lett.* **2006**, *3*, 29.

(44) Kresse, G.; Hafner, J. *Phys. Rev. B* **1994**, *49*, 14251.

(45) Chelikowsky, J.; Derby, J.; Godlevsky, V.; Jain, M.; Raty, J. *J. Phys.: Condens. Matter* **2001**, *13*, R817.

(46) Raty, J. Y.; Godlevsky, V.; Ghosez, P.; Bichara, C.; Gaspard, J. P.; Chelikowsky, J. R. *Phys. Rev. Lett.* **2000**, *85*, 1950.

(47) Li, J.; Drabold, D. A. *Phys. Rev. B* **2001**, *64*, 104206.

(48) Blaineau, S.; Jund, D. D. P. *Phys. Rev. B* **2003**, *67*, 094204.

(49) Tafen, D. N.; Drabold, D. A. *Phys. Rev. B* **2005**, *71*, 054206.

(50) Caravati, S.; Bernasconi, M.; Kühne, T. D.; Krack, M.; Parrinello, M. *Appl. Phys. Lett.* **2007**, *91*, 171906.

(51) Akola, J.; Jones, R. O. *Phys. Rev. B* **2007**, *76*, 235201.

(52) Akola, J.; Jones, R. O. *Phys. Rev. Lett.* **2008**, *100*, 205502.

(53) Errington, J. R.; Debenedetti, P. G. *Nature* **2001**, *409*, 318.

(54) Kolobov, A.; Fons, P.; Frenkel, A.; Ankudinov, A.; Tominaga, J.; Uruga, T. *Nat. Mater.* **2004**, *3*, 703.

(55) Kolobov, A.; Fons, P.; Tominaga, J.; Ankudinov, A.; Yannopoulos, S.; Andrikopoulos, K. *J. Phys.: Condens. Matter* **2004**, *16*, 5103.

(56) Jovari, P.; Kaban, I.; Steiner, J.; Beuneu, B.; Schöps, A.; Webb, M. A. *Phys. Rev. B* **2008**, *77*, 035202.

(57) Jovari, P.; Kaban, I.; Steiner, J.; Beuneu, B.; Schöps, A.; Webb, A. *J. Phys.: Condens. Matter* **2007**, *19*, 335212.

(58) Howard, W. E.; Tsu, R. *Phys. Rev. B* **1970**, *1*, 4709.

(59) Weidenhof, V.; Friedrich, I.; Ziegler, S.; Wuttig, M. *J. Appl. Phys.* **1999**, *86*, 5879.

(60) Wamwangi, D.; Njoroge, W.; Wuttig, M. *Thin Solid Films* **2002**, *408*, 310.

(61) Bichara, C.; Johnson, M.; Raty, J. *Phys. Rev. Lett.* **2005**, *95*, 267801.

(62) Christian, J. *Transformation in metals and alloys*, 2nd ed. Pergamon Press: Oxford, 1975.

(63) Jeong, T.; Kim, M.; Seo, H.; Kim, S.; Kim, S. *J. Appl. Phys.* **1999**, *86*, 774.

(64) Kalb, J.; Wen, C.; Spaepen, F.; Dieker, H.; Wuttig, M. *J. Appl. Phys.* **2005**, *98*, 054902.

(65) Kalb, J. In *Phase Change Materials: Science and Applications*; Raoux, S., Wuttig, M., Eds.; Springer: Berlin, Heidelberg, New York, 2008; Chapter 7, pp 125−148.

(66) Volmer, M. *Z. Elektrochem.* **1929**, *35*, 555.

(67) Becker, R.; Döring, W. *Ann. Phys.* **1935**, *24*, 719.

(68) Turnbull, D.; Fisher, J. *J. Chem. Phys.* **1949**, *17*, 71.

(69) Turnbull, D. *J. Appl. Phys.* **1950**, *21*, 1022.

(70) Thompson, C. V.; Spaepen, F. *Acta Metall.* **1979**, *27*, 1855.

(71) Hoffman, J. D. *J. Chem. Phys.* **1958**, *29*, 1192.

(72) Singh, H. B.; Holz, A. *Solid State Commun.* **1983**, *45*, 985.

(73) Kalb, J.; Spaepen, F.; Wuttig, M. *J. Appl. Phys.* **2005**, *98*, 054910.

(74) Senkader, S.; Wright, D. *J. Appl. Phys.* **2004**, *95*, 504.

(75) Kalb, J.; Spaepen, F.; Leervad Petersen, T. P.; Wuttig, M. *J. Appl. Phys.* **2003**, *94*, 4908.

(76) Wang, L.-M.; Angell, C. A.; Richert, R. *J. Chem. Phys.* **2006**, *125*, 074505.

(77) Kashchiev, D. *Surf. Sci.* **1969**, *14*, 209.

(78) Kalb, J.; Spaepen, F.; Wuttig, M. *J. Appl. Phys.* **2004**, *84*, 5240.

(79) Raoux, S.; Shelby, R.; Munoz, B.; Hitzbleck, M.; Krebs, D.; Salinga, M.; Woda, M.; Austgen, M.; Chung, K.-M.; Wuttig, M. Eur. Phase Change and Ovonic Sci. Symp., Prague, Czech Republic, Sept. 2008.

(80) Solis, J.; Afonso, C. N. *Appl. Phys. A: Mater. Sci. Process.* **2003**, *76*, 331.

(81) Yamada, N. *MRS Bull.* **1996**, *21*, 48.

(82) Stuke, J.; Zimmerer, G. *Phys. Status Solidi B-Basic Res.* **1972**, *49*, 513.

(83) Yamada, N.; Ohno, E.; Nishiuchi, K.; Akahira, N.; Takao, M. *J. Appl. Phys.* **1991**, *69*, 2849.

(84) Matsunaga, T.; Kubota, Y.; Yamada, N. *Acta Crystallogr. B* **2004**, *60*, 685.

(85) Matsunaga, T.; Umetani, Y.; Yamada, N. *Phys. Rev. B* **2001**, *64*, 184116.

(86) Njoroge, W.; Wöltgens, H.-W.; Wuttig, M. *J. Vac. Sci. Technol. A* **2002**, *20*, 230.

(87) Welnic, W.; Pamungkas, A.; Detemple, R.; Steimer, C.; Blügel, S.; Wuttig, M. *Nat. Mater.* **2006**, *5*, 56.

(88) Klein, A.; Dieker, H.; Späth, B.; Fons, P.; Kolobov, A.; Steimer, C.; Wuttig, M. *Phys. Rev. Lett.* **2008**, *100*, 016402.

(89) Welnic, W.; Botti, S.; Reining, L.; Wuttig, M. *Phys. Rev. Lett.* **2007**, *98*, 236403.

(90) Luo, M.; Wuttig, M. *Adv. Mater.* **2004**, *16*, 439.

(91) Detemple, R.; Wamwangi, D.; Wuttig, M.; Bihlmayer, G. *Appl. Phys. Lett.* **2003**, *83*, 2572.

(92) Lencer, D.; Salinga, M.; Grabowski, B.; Hickel, T.; Neugebauer, J.; Wuttig, M. *Nat. Mater.* **2008**, *7*, 972.

(93) Mott, N. F.; Davis, E. A. *Electronic processes in non-crystalline materials*; Clarendon Press: Oxford, 1979.

(94) Ielmini, D.; Sharma, D.; Lavizzari, S.; Lacaita, A. L. Proceedings of the International Reliability Physics Symposium, Phoenix, AZ; IRPS: 2008; p 597.

(95) Pirovano, A.; Lacaita, A. L.; Benvenuti, A.; Pellizzer, F.; Bez, R. *IEEE Trans. Electron Devices* **2004**, *51*, 452.

(96) Kato, T.; Tanaka, K. *Jpn. J. Appl. Phys.* **2005**, *44*, 7340.

(97) Street, R. A.; Mott, N. F. *Phys. Rev. Lett.* **1975**, *35*, 1293.

(98) Ielmini, D.; Zhang, Y. *Appl. Phys. Lett.* **2007**, *90*, 192102.

(99) Redaelli, A.; Ielmini, D.; Russo, U.; Lacaita, A. L. *J. Comput. Theor. Nanosci.* **2008**, *5*, 1183.

(100) Russo, U.; Ielmini, D.; Redaelli, A.; Lacaita, A. L. *IEEE Trans. Electron Devices* **2008**, *55*, 506.

(101) Ielmini, D.; Lacaita, A. L.; Mantegazza, D. *IEEE Trans. Electron Devices* **2007**, *54*, 308.

(102) Lacaita, A. L.; Redaelli, A.; Ielmini, D.; Pellizzer, F.; Pirovano, A.; Benvenuti, A.; Bez, R. *Int. Electron Devices Meeting Tech. Dig.* **2004**, 911.

(103) Ielmini, D.; Lacaita, A. L.; Pirovano, A.; Pellizzer, F.; Bez, R. *IEEE Electron Device Lett.* **2004**, *25*, 507.

(104) Russo, U.; Ielmini, D.; Redaelli, A.; Lacaita, A. L. *IEEE Trans. Electron Devices* **2006**, *53*, 3032.

(105) Redaelli, A.; Ielmini, D.; Russo, U.; Lacaita, A. L. *IEEE Trans. Electron Devices* **2006**, *53*, 3040.

(106) Ielmini, D.; Zhang, Y. *J. Appl. Phys.* **2007**, *102*, 054517.

(107) Ielmini, D. *Phys. Rev. B* **2008**, *78*, 035308.

(108) Hill, R. M. *Thin Solid Films* **1971**, *8*, R21.

(109) Ielmini, D.; Lavizzari, S.; Sharma, D.; Lacaita, A. L. *IEEE Trans. Electron Devices* **2009**, *56*, 1070.

(110) Jonscher, A. K.; Hill, R. M. In *Electrical conduction in disordered nonmetallic films*; Physics of Thin Films Vol. 8; Hass, G., Francombe, M. H., Hoffman, R. W., Eds.;Academic Press: 1975.

(111) Emin, D.; Seager, C. H.; Quinn, R. K. *Phys. Rev. Lett.* **1972**, *28*, 813.

(112) Emin, D. *Phys. Rev. B* **2006**, *74*, 035206.

(113) Warren, A. C. *IEEE Trans. Electron Devices* **1973**, *20*, 123.

(114) Adler, D.; Shur, M. S.; Silver, M.; Ovshinsky, S. R. *J. Appl. Phys.* **1980**, *51*, 3289.

(115) Karpov, I. V.; Mitra, M.; Kau, D.; Spadini, G.; Kryukov, Y. A.; Karpov, V. G. *J. Appl. Phys.* **2007**, *102*, 124503.

(116) Jonscher, A. K. *J. Phys. C* **1971**, *4*, 1331.

(117) Wolfe, C. M., Jr.; Stillman, G. E. *Physical properties of semiconductors*; Prentice Hall: Upper Saddle River, NJ, 1989.

(118) Hindley, N. K. *J. Non Crystalline Solids* **1970**, *5*, 31.

(119) Buckley, W. D.; Holmberg, S. H. *Phys. Rev. Lett.* **1974**, *32*, 1429.

(120) Lavizzari, S.; Ielmini, D.; Sharma, D.; Lacaita, A. L. *Int. Electron Devices Meeting Tech. Dig.* **2008**, 215.

(121) Degraeve, R.; Groeseneken, G.; Bellens, R.; Ogier, J. L.; Depas, M.; Roussel, P. J.; Maes, H. E. *IEEE Trans. Electron Devices* **1998**, *45*, 904.

(122) Fantini, P.; Pirovano, A.; Ventrice, D.; Redaelli, A. *Appl. Phys. Lett.* **2006**, *88*, 263506.

(123) Fantini, P.; Betti Beneventi, G.; Calderoni, A.; Larcher, L.; Pavan, P.; Pellizzer, F. *Int. Electron Devices Meeting Tech. Dig.* **2008**, 219.

(124) Mantegazza, D.; Ielmini, D.; Varesi, E.; Pirovano, A.; Lacaita, A. L. *Int. Electron Devices Meeting Tech. Dig.* **2007**, 311.

(125) Ohshima, N. *J. Appl. Phys.* **1996**, *79*, 8357.

(126) Martens, H. C. F.; Vlutters, R.; Prangsma, J. C. *J. Appl. Phys.* **2004**, *95*, 3977.

(127) Zhou, G.-F.; Jacobs, B. A. J. *Jpn. J. Appl. Phys.* **1999**, *38*, 1625.

(128) Zhou, G.-F. *Mater. Sci. Eng., A* **2001**, *304*−*306*, 73.

(129) Wang, W. J.; Shi, L. P.; Zhao, R.; Lim, K. G.; Lee, H. K.; Chong, T. C.; Wu, Y. H. *Appl. Phys. Lett.* **2008**, *93*, 043121.

(130) Lee, S.-H.; Jung, Y.; Agarwal, R. *Nano Lett.* **2008**, *8*, 3303.

(131) Sokolowski-Tinten, K.; Solis, J.; Bialkowski, J.; Siegel, J.; Afonso, C. N.; von der Linde, D. *Phys. Rev. Lett.* **1998**, *81*, 3679.

(132) Wiggins, S. M.; Gawelda, W. M.; Solis, J.; Serna, R.; Afonso, C. N. *J. Appl. Phys.* **2003**, *94*, 4961.

(133) Raoux, S.; Shelby, R. M.; Jordan-Sweet, J.; Munoz, B.; Salinga, M.; Chen, Y.-C.; Shih, Y.-H.; Lai, E.-K.; Lee, M.-H. *Microelectron. Eng.* **2008**, *85*, 2330.

(134) Sun, X.; Yu, B.; Ng, G.; Meyyappan, M. *J. Phys. Chem. C* **2007**, *111*, 2421.

(135) Milliron, D. Mater. Res. Soc. Spring Meeting, San Francisco, CA, 2008.

(136) Caldwell, M.; Raoux, S.; Milliron, D. J.; Wong, H.-S. P. 234th Am. Chem. Soc. Meeting, Boston, MA, 2007.

(137) Caldwell, M. *Particles*, paper no. 120, Orlando, FL, 2008.

(138) Gleixner, B.; Pirovano, A.; Sarkar, J.; Ottogalli, F.; Tortorelli, I.; Tosi, M.; Bez, R. *Proceedings of the International Reliability Physics Symposium*, Phoenix, AZ, 2007; p 542.

(139) Khonik, V. A.; Kitagawa, K.; Morii, H. *J. Appl. Phys.* **2000**, *87*, 8440.

(140) Wei, X.; Shi, L.; Chong, T. C.; Zhao, R.; Lee, H. K. *Jpn. J. Appl. Phys.* **2007**, *46*, 2211.

(141) Raoux, S.; Jordan-Sweet, J.; Kellock, A. *J. Appl. Phys.* **2008**, *103*, 114310.

(142) Raoux, S.; Cheng, H.-Y.; Jordan-Sweet, J. L.; Munoz, B.; Hitzbleck, M. *Appl. Phys. Lett.* **2009**, *94*, 183114.

(143) Knaepen, W.; Detavernier, C.; Van Meirhaeghe, R. L.; Jordan-Sweet, J.; Lavoie, C. *Thin Solid Films* **2008**, *516*, 4946.

(144) Raoux, S.; Rettner, C. T.; Jordan-Sweet, J. L.; Kellock, A. J.; Topuria, T.; Ride, P. M.; Miller, D. *J. Appl. Phys.* **2007**, *102*, 094305.

(145) Raoux, S.; Zhang, Y.; Milliron, D.; Cha, J.; Caldwell, M.; Rettner, C. T.; Jordan-Sweet, J. L.; Wong, H.-S. P. *European Phase Change and Ovonic Science Symposium,* Zermatt, Switzerland, 2007.

(146) Zhang, Y.; Wong, H.-S. P.; Raoux, S.; Cha, J. N.; Rettner, C. T.; Krupp, L. E.; Topuria, T.; Milliron, D.; Rice, P. M.; Jordan-Sweet, J. L. *Appl. Phys. Lett.* **2007**, *91*, 013104.

(147) Zhang, Y.; Raoux, S.; Krebs, D.; Krupp, L. E.; Topuria, T.; Caldwell, M. A.; Milliron, D.; Kellock, A.; Rice, P. M.; Jordan-Sweet, J. L.; Wong, H.-S. P. *J. Appl. Phys.* **2008**, *104*, 074312.

(148) Milliron, D. J.; Raoux, S.; Shelby, R. M.; Jordan-Sweet, J. *Nat. Mater.* **2007**, *6*, 352.

(149) Miao, X. S.; Chong, T. C.; Huang, Y. M.; Lim, K. G.; Tan, P. K.; Shi, L. P. *Jpn. J. Appl. Phys.* **1999**, *38*, 1638.

(150) Reifenberg, J. P.; Panzer, M. A.; Kim, S.-B.; Gibby, A. M.; Zhang, Y.; Wong, S.; Wong, H.-S. P.; Pop, E.; Goodson, K. E. *Appl. Phys. Lett.* **2007**, *91*, 111904.

(151) Lankhorst, M. H. R.; Ketelaars, B. W. S. M. M.; Wolters, R. A. M. *Nat. Mater.* **2005**, *4*, 347.

(152) Jedema, F. J.; Zandt, M. A. A.; Wolters, R. A. M.; Delhougne, R.; Gravesteijn, D. J.; Tio Castro, D.; Hurkx, G. A. M.; Attenborough, K. *European Phase Change and Ovonic Science Symposium,* Zermatt, Switzerland, paper E02, 2007.

(153) Krebs, D.; Raoux, S.; Rettner, C. T.; Shelby, R. M.; Burr, G. W.; Wuttig, M. Mater. Res. Soc. Proc. 2008, *1072*, paper 1072-G06-07.

(154) Gotoh, T.; Sugawara, K.; Tanaka, K. *Jpn. J. Appl. Phys.* **2004**, *43*, L818.

(155) Satoh, H.; Sugawara, K.; Tanaka, K. *J. Appl. Phys.* **2006**, *99*, 024306.

(156) Gidon, S.; Lemonnier, O.; Rolland, B.; Bichet, O.; Dressler, C.; Samson, Y. *Appl. Phys. Lett.* **2004**, *85*, 6392.

(157) Hamann, H.; O'Boyle, M.; Martin, Y.; Rooks, M.; Wickramasinghe, H. K. *Nat. Mater.* **2006**, *5*, 383.

(158) Wright, C. D.; Armand, M.; Aziz, M. M. *IEEE Trans. Nanotechnol.* **2006**, *5*, 50.

(159) Shi, L. In *Phase Change Materials: Science and Applications*; Raoux, S., Wuttig, M., Eds.; Springer: Berlin, Heidelberg, New York, 2008; Chapter 12, pp 253−284.

(160) Yamada, N.; Kojima, R.; Uno, M.; Kitaura, H.; Narumi, K.; Nishiuchi, K. *Proc. SPIE* **2002**, *4342*, 55.

(161) Welnic, W.; Wuttig, M. *Today* **2008**, *11*, 20.

(162) Hayashi, S.; Kino, G. S.; Ichimura, I. *Proc. SPIE* **1995**, *2412*, 80.

(163) Terris, B. D.; Mamin, H. J.; Rugar, D.; Studenmund, W. R.; Kino, G. S. *Appl. Phys. Lett.* **1994**, *65*, 388.

(164) Wu, Q.; Feke, G. D.; Grober, R. D.; Ghislain, L. P. *Appl. Phys. Lett.* **1999**, *75*, 4064.

(165) Nakano, T.; Sato, A.; Fuji, H. *Appl. Phys. Lett.* **1999**, *75*, 151.

(166) Tominaga, J.; Fuji, H.; Sato, A.; Nakano, T.; Atoda, N. *Jpn. J. Appl. Phys.* **2000**, *39*, 957.

(167) Kim, J.; Hwang, I.; Yoon, D.; Park, I.; Shin, D.; Kuwahara, M.; Tominaga, J. *Jpn. J. Appl. Phys.* **2003**, *42*, 1014.

(168) Shima, T.; Nakano, T.; Kim, J.; Tominaga, J. *Jpn. J. Appl. Phys.* **2005**, *44*, 3631.

(169) Neale, R. G.; Nelson, D. L.; Moore, G. E. *Electronics* **1970**, *43*, 56.

(170) Oh, J. H.; Park, J. H.; Lim, Y. S.; Lim, H. S.; Oh, Y. T.; Kim, J. S.; Shin, J. M.; Park, J. H.; Song, Y. J.; Ryoo, K. C.; Lim, D. W.; Park, S. S.; Kim, J. I.; Kim, J. H.; Yu, J.; Yeung, F.; Jeong, C. W.; Kong, J. H.; Kang, D. H.; Koh, G. H.; Jeong, G. T.; Jeong, H. S.; Kim, K. *Int. Electron. Devices Meeting*, San Francisco, CA, 2006; p 49.

(171) Ahn, S. J.; Hwang, Y. N.; Song, Y. J.; Lee, S. H.; Leee, S. Y.; Park, J. H.; Jeong, C. W.; Ryoo, K. C.; Shin, J. M.; Park, J. H.; Fai, Y.; Oh, J. H.; Koh, G. H.; Jeong, G. T.; Joo, S. H.; Choi, S. H.; Son, Y. H.; Shin, J. C.; Kim, Y. T.; Jeong, H. S.; Kim, K. *Symp. on VLSI Tech. Dig.*, Washington, DC, 2005; pp 98−99.

(172) Ha, Y. H.; Yi, J. H.; Horii, H.; Park, J. H.; Joo, S. H.; Park, S. O.; Chung, U.-I.; Moon, J. T. *Symp. on VLSI Tech. Dig.*, 2003; pp 175−176.

(173) Pellizzer, F.; Pirovano, A.; Ottogalli, F.; Magistretti, M.; Scaravaggi, M.; Zuliani, P.; Tosi, M.; Ben-venuti, A.; Besana, P.; Cadeo, S.; Marangon, T.; Morandi, R.; Piva, R.; Spandre, A.; Zonca, R.; Modelli, A.; Varesi, E.; Lowrey, T.; Lacaita, A.; Casagrande, G.; Cappelletti, P.; Bez, R. *Symp. on VLSI Tech. Dig.,* 2004; pp 18−19.

(174) Breitwisch, M.; Nirschl, T.; Chen, C. F.; Zhu, Y.; Lee, M. H.; Lamorey, M.; Burr, G. W.; Joseph, E.; Schrott, A.; Philipp, J. B.; Cheek, R.; Happ, T. D.; Chen, S. H.; Zaidi, S.; Flaitz, P.; Bruley, J.; Dasaka, R.; Rajendran, B.; Rossnagel, S.; Yang, M.; Chen, Y. C.; Bergmann, R.; Lung, H. L.; Lam, C. Novel lithography-independent pore phase change memory. *Symposium on VLSI Technology*; 2007; p 6B-3.

(175) Happ, T. D.; Breitwisch, M.; Schrott, A.; Philipp, J. B.; Lee, M. H.; Cheek, R.; Nirschl, T.; Lamorey, M.; Ho, C. H.; Chen, S. H.; Chen, C. F.; Joseph, E.; Zaidi, S.; Burr, G. W.; Yee, B.; Chen, Y. C.; Raoux, S.; Lung, H. L.; Bergmann, R.; Lam, C. *Symp. on VLSI Technol. Dig.,* Honolulu, Hawaii, 2006; pp 15−16.

(176) Chen, Y. C.; Rettner, C. T.; Raoux, S.; Burr, G. W.; Chen, S. H.; Shelby, R. M.; Salinga, M.; Risk, W. P.; Happ, T. D.; McCleland, G. M.; Breitwisch, M.; Schrott, A.; Philipp, J. B.; Lee, M. H.; Cheek, R.; Nirschl, T.; Lamorey, M.; Chen, C. F.; Joseph, E.; Zaidi, S.; Yee, B.; Lung, H. L.; Bergmann, R.; Lam, C. *Int. Electron. Devices Meeting Tech. Dig.*, 2006; pp 777−780.

(177) Chen, Y.-C. In *Phase Change Materials: Science and Applications*; Raoux, S., Wuttig, M., Eds.; Springer: Berlin, Heidelberg, New York, 2008; Chapter 15, pp 331−354.

(178) Bez, R.; Gleixner, R. J.; Pellizzer, F.; Pirovano, A.; Atwood, G. In *Phase Change Materials: Science and Applications*; Raoux, S., Wuttig, M., Eds.; Springer: Berlin, Heidelberg, New York, 2008; Chapter 16, pp 355−380.

(179) Breitwisch, M. In *Phase Change Materials: Science and Applications*; Raoux, S., Wuttig, M., Eds.; Springer: Berlin, Heidelberg, New York, 2008; Chapter 17, pp 381−408.

(180) Lai, S. *IBM J. Res. Dev.* **2008**, *52*, 529.

(181) http://news.cnet.com/Bye-bye-hard-drive,-hello-flash/2100-1006_3-6005849.html.

(182) Freitas, R. F.; Wilcke, W. W. *J. Res. Dev.* **2008**, *52*, 439.

(183) Burr, G. W.; Kurdi, B. N.; Scott, J. C.; Lam, C. H.; Gopalakrishnan, K.; Shenoy, R. S. *IBM J. Res. Dev.* **2008**, *52*, 449.

(184) http://ovonyx.com/technology/technology.pdf.

(185) Lyke, J. In *Phase Change Materials: Science and Applications*; Raoux, S., Wuttig, M., Eds.; Springer: Berlin, Heidelberg, New York, 2008; Chapter 18, pp 409−430.

(186) Nirschl, T.; Philipp, J. B.; Happ, T. D.; Burr, G. W.; Rajendran, B.; Lee, M. H.; Schrott, A.; Yang, M.; Breitwisch, M.; Chen, C. F.; Joseph, E.; Lamorey, M.; Cheek, R.; Chen, S. H.; Zaidi, S.; Raoux, S.; Chen, Y. C.; Zhu, Y.; Bergmann, R.; Lung, H. L.; Lam, C. *Int. Electron Devices Meeting*, Washington, DC, 2007.

(187) Ovshinsky, R. *European Phase Change and Ovonic Science Symp.*, Balzers, Liechtenstein, 2004.

(188) Ovshinsky, S. R.; Pashmakov, B. Mater. Res. Soc. Symp. Proc., 2004, Vol. 803, paper HH1.1.1.

(189) Ovshinsky, S. R. *Jpn. J. Appl. Phys.* **2004**, *43*, 4695.

(190) Wright, C. D.; Blyuss, K.; Ashwin, P. *European Phase Change and Ovonic Science Symp.*, Zermatt, Switzerland, 2007.

(191) http://www-03.ibm.com/press/us/en/pressrelease/26123.wss.

(192) Milliron, D.; Huang, Q.; Zhu, Y. In *Phase Change Materials: Science and Applications*; Raoux, S., Wuttig, M., Eds.; Springer: Berlin, Heidelberg, New York, 2008; Chapter 11, pp 227−248.

CR900040X